

# 1 Measurement report: Assessing the Impacts of Emission Uncertainty 2 on Aerosol Optical Properties and Radiative Forcing from Biomass 3 Burning in Peninsular Southeast Asia

4 Yinbao Jin<sup>1</sup>, Yiming Liu\*<sup>1</sup>, Xiao Lu<sup>1</sup>, Xiaoyang Chen<sup>2</sup>, Ao Shen<sup>1</sup>, Haofan Wang<sup>1</sup>, Yinping Cui<sup>1</sup>, Yifei  
5 Xu<sup>1</sup>, Siting Li<sup>1</sup>, Jian Liu<sup>1</sup>, Ming Zhang<sup>4</sup>, Yingying Ma<sup>3</sup>, Qi Fan\*<sup>1,5,6</sup>

6 <sup>1</sup>School of Atmospheric Sciences, Sun Yat-Sen University, Zhuhai 519082, China

7 <sup>2</sup>Institute of Tropical and Marine Meteorology, China Meteorological Administration, Guangzhou, 510000, China

8 <sup>3</sup>State Key Laboratory of Information Engineering in Surveying, Mapping and Remote-sensing, Wuhan University, Wuhan  
9 430079, China

10 <sup>4</sup>Hubei Key Laboratory of Critical Zone Evolution, School of Geography and Information Engineering, China University of  
11 Geosciences, Wuhan 430074, China

12 <sup>5</sup>Southern Marine Science and Engineering Guangdong Laboratory, Zhuhai 519082, China

13 <sup>6</sup>Guangdong Province Key Laboratory for Climate Change and Natural Disaster Studies, School of Atmospheric Sciences, Sun  
14 Yat-sen University, Guangzhou 510275, China

15  
16 *Correspondence to:* Qi Fan (eesfq@mail.sysu.edu.cn) and Yiming Liu (liuym88@mail.sysu.edu.cn)

## 17 **Abstract.**

18 Despite significant advancements in improving the dataset for biomass burning (BB) emissions over the past few decades,  
19 uncertainties persist in BB aerosol emissions, impeding the accurate assessment of simulated aerosol optical properties (AOPs)  
20 and direct radiative forcing (DRF) during wildfire events in global and regional models. This study assessed AOPs (including  
21 aerosol optical depth (AOD), aerosol absorption optical depth (AAOD), and aerosol extinction coefficients (AEC)) and DRF  
22 using eight independent BB emission inventories applied to the WRF-Chem model during the BB period (March 2019) in  
23 Peninsular Southeast Asia (PSEA), where the eight BB emission inventories were the Global Fire Emissions Database version  
24 4.1s (GFED), Fire INventory from NCAR version 1.5 (FINN1.5), the Fire Inventory from NCAR version 2.5 MOS (MODIS  
25 fire detections, FINN2.5 MOS), the Fire Inventory from NCAR version 2.5 MOSVIS (MODIS+VIIRS fire detections,  
26 FINN2.5 MOSVIS), Global Fire Assimilation System version 1.2s (GFAS), Fire Energetics and Emissions Research version  
27 1.0 (FEER), Quick Fire Emissions Dataset version 2.5 release 1 (QFED), and Integrated Monitoring and Modelling System  
28 for Wildland FIRES Project version 2.0 (IS4FIRES), respectively. The results show that in the PSEA region, organic carbon  
29 (OC) emissions in the eight BB emission inventories differ by a factor of about 9 (0.295-2.533 Tg/M), with  $1.09 \pm 0.83$  Tg/M  
30 and a coefficient of variation (CV) of 76%. High-concentration OC emissions occurred primarily in savanna and agricultural  
31 fires. The OC emissions from the GFED and GFAS are significantly lower than the other inventories. The OC emissions in  
32 FINN2.5 VISMOS are approximately twice as high as those in FINN1.5. Sensitivity analysis of AOD simulated by WRF-  
33 Chem to different BB emission datasets indicated that the FINN scenarios (v1.5 and 2.5) significantly overestimate AOD  
34 compared to observation (VIIRS), while the other inventories underestimate AOD in the high AOD (HAOD, AOD>1) regions



35 range from 97-110°E, 15-22.5°N. Among the eight schemes, IS4FIRES and FINN1.5 performed better in terms of AOD  
36 simulation consistency and bias in the HAOD region when compared to AERONET sites. The AAOD in WRF-Chem during  
37 the PSEA wildfire period was assessed using satellite observations (TROPOMI) and AERONET data, and it was found that  
38 the AAOD simulated with different BB schemes did not perform as well as the AOD. The significant overestimation of AAOD  
39 by FINN (v1.5 and 2.5), FEER, and IS4FIRES schemes in the HAOD region, with the largest overestimation for FINN2.5  
40 MOSVIS. FINN1.5 schemes performed better in representing AAOD at AERONET sites within the HAOD region. The  
41 simulated AOD and AAOD from FINN2.5 MOSVIS always show the best correlation with the observations. AEC simulated  
42 by WRF-Chem with all the eight BB schemes trends were consistent with CALIPSO in the vertical direction (0.5 km to 4 km),  
43 demonstrating the efficacy of the smoke plume rise model used in WRF-Chem to simulate smoke plume heights. However,  
44 the FINN (v1.5 and 2.5) schemes overestimated AEC, while the other schemes underestimated it. In the HAOD region, BB  
45 aerosols exhibited a daytime shortwave radiative forcing of  $-32.60 \pm 24.50 \text{ W/m}^2$  at the surface, positive forcing ( $1.70 \pm 1.40$   
46  $\text{W/m}^2$ ) in the atmosphere, and negative forcing ( $-30.89 \pm 23.6 \text{ W/m}^2$ ) at the top of the atmosphere. Based on the analysis,  
47 FINN1.5 and IS4FIRES are recommended for accurately assessing the impact of BB on air quality and climate in the PSEA  
48 region.

## 49 **1 Introduction**

50 Peninsular Southeast Asia (PSEA), including Vietnam, Thailand, Myanmar, Cambodia, and Laos, is one of the major biomass  
51 burning (BB) emission source areas in the world (Yadav et al., 2017). Due to widespread forest fires and agro-residue burning,  
52 extensive BB activities occur over PSEA, especially during the dry season (BB usually peaks in March) (Reddington et al.,  
53 2021) and release large amounts of aerosols and trace gases (including organic carbon (OC), black carbon (BC), particulate  
54 matter (PM), nitrogen oxides ( $\text{NO}_x$ ), and volatile organic compounds (VOC)) into the air, thus leading to significant impacts  
55 on atmospheric composition, radiative budget, and human health (Reid et al., 2013). Therefore, it is crucial to understand the  
56 BB emission inventories, as well as the behavior of aerosols, and accurately model their properties, to assess their impact on  
57 air quality and climate change in the PSEA region.

58 Numerous studies have been conducted to assess the effects of BB emissions on aerosol optical properties (AOPs), such as  
59 aerosol optical depth (AOD), absorbing aerosol optical depth (AAOD), and aerosol extinction coefficient (AEC), as well as  
60 direct radiative forcing (DRF) in the PSEA region (Zhu et al., 2017; Lin et al., 2014; Dong and Fu, 2015a). However, most of  
61 these studies have relied on only one single BB emission inventory without comparing different inventories, leading to large  
62 uncertainties in assessing the impact of BB aerosols. Due to the challenges in directly measuring BB emissions, various global  
63 fire emissions inventories have been developed based on satellite observations in the past decades (Ichoku and Ellison, 2014;  
64 Wiedinmyer et al., 2023; Wiedinmyer et al., 2011). These inventories use different empirical methods and underlying data to  
65 represent gas and aerosol emissions from fires, resulting in inherent uncertainties (Carter et al., 2020).



66 These uncertainties arising from different BB emissions often manifest as regional variations and inconsistencies with  
67 observations when integrated into models (Liu et al., 2020). Addressing these uncertainties is crucial for refining climate  
68 models and providing more accurate projections of future climate change. For example, Pan et al. (2020) compared six BB  
69 aerosol emission datasets from 2008 globally as well as from 14 regions, and the total global emissions from these BB emission  
70 datasets differed by a factor of 3.8. Sensitivity analysis of AOD simulated by Goddard Earth Observing System-Chemistry  
71 (GEOS-Chem) to different BB emission datasets during the peak BB period in each region and at most AERONET sites in  
72 each region found that Quick Fire Emissions Dataset version 2.4 (QFED2.4) produced the highest AOD values, closest to  
73 observations, followed closely by Fire Energetics and Emissions Research version 1.0 (FEER1.0). In the North American  
74 region, the GEOS-Chem incorporating four different BB emission inventories and remote-sensing data analysis during wildfire  
75 periods indicated a 4 to 7-fold difference in BB aerosol emissions. Simulations driven by Global Fire Emissions Database  
76 version 4s (GFED4s) and Global Fire Assimilation System version 1.2 (GFAS1.2) provide better agreement with surface  
77 measurements of organic aerosol and BC mass concentrations, BC observations at higher altitudes, and Moderate Resolution  
78 Imaging Spectroradiometer (MODIS) observations of AOD (Carter et al., 2020). To explore the uncertainty of BB emissions  
79 in the tropics, GFED V3, Fire INventory from NCAR version 1 (FINN1.0), and GFAS1 were used to evaluate Global Model  
80 of Aerosol Processes (GLOMAP) model simulations of AOD in South America, Africa, and Southeast Asia showing that the  
81 model underestimates AOD for all emission datasets (Reddington et al., 2016). In the North Sub-Saharan Africa BB region,  
82 Zhang et al. (2014) found a 12-fold difference in estimates of total smoke emissions and an even larger difference (up to 33-  
83 fold) in WRF-Chem simulated smoke-related variables and radiative effects. Recent studies have shown that during the PSEA  
84 march BB peak, only the FINN2.5 captures the feature, which is not seen in GFED and as pronounced in other inventories  
85 (Wiedinmyer et al., 2023). Despite substantial research efforts, accurately representing BB aerosols in models remains a  
86 challenge. In summary, compared to the differences between global BB emission inventories, regional differences may be  
87 larger, especially in the PSEA region, where the satellite inversions of BB contain a large fraction of uncertainty due to high  
88 cloud cover (Dong and Fu, 2015b). Significant differences exist in AOPs and radiative forcing simulated by different emission  
89 inventories in the high BB emission region within a single model (Carter et al., 2020; Zhang et al., 2014). To reduce  
90 uncertainties, it is necessary to compare the differences between commonly used BB emission inventories and evaluate the  
91 model simulations of AOPs and radiative effects for the PSEA region.

92 In March 2019, the National Aeronautics and Space Administration (NASA) used remote sensing data from Visible Infrared  
93 Imaging Radiometer Suite (VIIRS) to discover hundreds of fires burning in the PSEA region (Jenner, Mar 18, 2019). Therefore,  
94 this study aims to analyze how emission uncertainties or differences from different BB inventories affect the spatial and  
95 temporal distribution of aerosols and their radiative effects in the PSEA region. Section 2 describes the model configuration,  
96 experimental design, and data sources. Section 3 presents a comparison of eight emission inventories in March 2019 and the  
97 results of simulating AOPs and DRF. Discussions are provided in Section 4, and the study concludes with a summary in  
98 Section 5.



## 99 2 Data and Methods

### 100 2.1 Model Description and Configuration

#### 101 2.1.1 WRF-Chem

102 The simulations were conducted using version 3.9.1.1 of the WRF-Chem online-coupled meteorology and chemistry model  
103 (Grell et al., 2005). A single domain (Figure 1) was employed, mainly focusing on the PSEA region (red line, including  
104 Vietnam, Thailand, Myanmar, Cambodia, and Laos,) and studying BB from February 26th to March 31st, 2019. The initial 3  
105 days of the model simulation were used as a spin-up period. The model consisted of 27 vertical layers and one nested horizontal  
106 resolution of 27 x 27 km. The selected physical configurations included the Morrison double-moment microphysics scheme  
107 (Morrison et al., 2005), the Rapid Radiation Transfer Model (RRTMG) longwave and shortwave radiation schemes (Iacono et  
108 al., 2008), the Mellor-Yamada-Janjic (MYJ) planetary boundary layer scheme (Mellor and Yamada, 1982; Janjić, 1990), the  
109 Eta similarity surface Layer scheme (Monin and Obukhov, 1954), the Noah Land Surface Model land surface scheme (Niu et  
110 al., 2011) and the Grell 3D cumulus parameterization scheme (Grell and Dévényi, 2002). The Model for Ozone and Related  
111 chemical Tracers (MOZART) trace gas chemistry with the Model for Simulating Aerosol Interactions and Chemistry  
112 (MOSAIC with 4 bins) aerosol scheme with the Kinetic Preprocessor (KPP) library is used in the model (Emmons et al.,  
113 2010). In this study, MOSAIC uses a sectional approach to represent aerosol size distributions with four discrete size bins with  
114 glyoxal uptake into aqueous aerosols to form secondary organic aerosol (SOA) in the PSEA region by WRF-Chem, which is  
115 capable of simulating all major aerosol components, including nitrates ( $NO_3^-$ ), sulfates ( $SO_4^{2-}$ ), ammonium ( $NH_4^+$ ), BC,  
116 primary organic aerosols, and other inorganic aerosols, with high efficiency and accuracy for use in air quality and  
117 regional/global aerosol modeling (Zhang et al., 2018). The Community Atmosphere Model with Chemistry (CAM-chem)  
118 simulation outputs (Emmons et al., 2020; Buchholz et al., 2019) are used as chemical lateral boundary and initial conditions  
119 for WRF-Chem (<https://rda.ucar.edu/datasets/ds313.7/>, last access: 11 May 2023). The product simulated by CAM-chem has  
120 a horizontal resolution of 0.9 degrees by 1.25 degrees and 56 vertical levels in the vertical direction. Meteorological initial and  
121 boundary conditions were obtained from the National Centers for Environmental Prediction Final Analysis data with a 1° x 1°  
122 horizontal resolution.

123 WRF-Chem employs Mie theory to perform calculations of AOPs using MOSAIC size distributions and the complex refractive  
124 indices associated with each MOSAIC chemical constituent. Specifically, it simulates AOPs (such as AEC, single scattering  
125 albedo (SSA), and asymmetry factor for scattering) distributed in four different bands: 300, 400, 600, and 1000 nm. This study  
126 used the Ångström power law (Ångström, 1929; Martinez-Lozano et al., 1998) to derive the model at 550 nm for AOD, and  
127 the detailed calculation procedure follows Kumar et al. (2014) and Saide et al. (2013). In addition, the aerosol direct radiative  
128 feedback was coupled with the RRTMG for both shortwave (SW) and longwave (LW) radiation as implemented by Zhao et  
129 al. (2010). A detailed description of the computation of AOPs and DRF in WRF-Chem has been given by Fast et al. (2006),  
130 Zhao et al. (2011), and Lin et al. (2014).



## 131 **2.1.2 Anthropogenic and Biogenic Emissions**

132 The latest version of the global anthropogenic emissions inventory, the monthly Emissions Database for Global Atmospheric  
133 Research (EDGAR) v5.0, was published by Marvin (2022) on February 17, 2022. It provides global air pollutant emissions  
134 for the year 2015 at a resolution of  $0.1^\circ \times 0.1^\circ$ . These emissions were speciated for the MOZART chemical mechanism and can  
135 be accessed at <https://zenodo.org/record/6130621> (last accessed on 11 May 2023). Biogenic emissions were calculated online  
136 within the model using the Model of Emissions of Gases and Aerosols from Nature (MEGAN) inventory developed by  
137 Guenther et al. (2012).

## 138 **2.2 BB Emission Inventories**

139 There are two primary approaches to estimating BB emission inventories: "bottom-up" and "top-down" methods (Archer-  
140 Nicholls et al., 2015). The "bottom-up" approach involves estimating emissions per species by multiplying emission factors  
141 (EF) with estimates of the biomass burned (Yevich and Logan, 2003). The latter, the "top-down" approach, bypasses the largely  
142 uncertain fuel consumption estimation step by estimating emission fluxes directly from fire radiative power (FRP) (Ichoku  
143 and Ellison, 2014). The "top-down" approach commonly utilizes AOD retrieved from satellite remote sensing to constrain  
144 aerosol emissions from wildfires (Huneeus et al., 2012). This study evaluates the performance of the WRF-Chem using eight  
145 different BB emission inventories to simulate wildfires in the PSEA region during March 2019. These emission inventories  
146 include the Global Fire Emissions Database version 4.1s (GFED), Fire INventory from NCAR version 1.5 (FINN1.5), the Fire  
147 Inventory from NCAR version 2.5 MOS (MODIS fire detections, FINN2.5 MOS), the Fire Inventory from NCAR version 2.5  
148 MOSVIS (MODIS+VIIRS fire detections, FINN2.5 MOSVIS), Global Fire Assimilation System version 1.2s (GFAS), Fire  
149 Energetics and Emissions Research version 1.0 (FEER), Quick Fire Emissions Dataset version 2.5 release 1 (QFED), and  
150 Integrated Monitoring and Modelling System for Wildland FIRES Project version 2.0 (IS4FIRES). Table 1 provides a detailed  
151 comparison of their spatial and temporal resolution, the main references for the EF, the satellite data sources, Non-methane  
152 hydrocarbons (NMHCs), oxygen volatile organic compounds (OVOCs), gas, and aerosols in the inventory. NMHCs refer to  
153 organic compounds containing only C and H besides methane ( $\text{CH}_4$ ), such as alkanes, alkenes, alkynes, etc. OVOCs contain  
154 C, H, and O compounds, e.g., alcohols, aldehydes, ketones, etc. NMHCs and OVOCs combined constitute nearly all of the  
155 non-methane volatile organic compounds (NMVOCs) emitted by wildfires (Akagi et al., 2011).

### 156 **2.2.1 GFED (v4.1s)**

157 The GFED4.1s datasets provide the area burned, dry matter (DM), and EF from global fires. It has a spatial resolution of  $0.25^\circ$   
158  $\times 0.25^\circ$  and can be accessed at [https://daac.ornl.gov/get\\_data/](https://daac.ornl.gov/get_data/) (last accessed on 11 May 2023). This dataset includes fractional  
159 contributions from different fire types and offers daily or 3-hourly data to scale monthly emissions to a higher temporal  
160 resolution. GFED4.1s is an enhanced version of the GFED4 dataset, incorporating small fire inputs to enhance the accuracy  
161 and completeness of emission estimates (Randerson et al., 2017). It covers the period from June 1997 to 2022 and includes a



162 wide range of emission species such as carbon (C), DM, carbon dioxide (CO<sub>2</sub>), carbon monoxide (CO), methane (CH<sub>4</sub>),  
163 hydrogen (H<sub>2</sub>), nitrous oxide (N<sub>2</sub>O), NO<sub>x</sub>, NMHCs, OVOCs, OC, BC, PM less than 2.5 microns in diameter (PM<sub>2.5</sub>), total PM  
164 (TPM), and sulfur dioxide (SO<sub>2</sub>). The raw GFED emission data (0.25°x 0.25°) were first re-gridded to the required spatial  
165 resolution for the WRF-Chem domains using the Earth System Modeling Framework (EMSF) program in Figure 2, followed  
166 by supplementing the GFED emission species (Table S1) to meet the MOZART-MOSAIC scheme based on the study by  
167 Akagi et al. (2011) and Heil A. (2020). The construction of the final emission inventory included incorporating the mean  
168 fraction and fire size of the four vegetation types (grassland, extratropical forest, savanna, tropical forest) from FINN1.5. This  
169 incorporation enables WRF-Chem to calculate the smoke plume rise (Freitas et al., 2007; 2010).

### 170 **2.2.2 FINN (v1.5, v2.5 MOS, and v2.5 MOSVIS)**

171 The emissions estimation of FINN (v1.5 and 2.5 ) are based on the framework described by Wiedinmyer et al. (2011) and  
172 Wiedinmyer et al. (2023), which utilizes two types of satellite observations: (1) MODIS fire detections and (2) active fire  
173 detections from both MODIS and VIIRS. It provides global daily estimates of BB emissions for important gases and aerosols,  
174 along with comprehensive specifications of total VOC emissions for three commonly used chemical mechanisms (MOZART-  
175 T1, SAPRC99, and GEOS-Chem) in regional and global chemical transport models (<https://www.acom.ucar.edu/Data/fire/>,  
176 last accessed on 11 May 2023). Since its release, FINN has been widely utilized by researchers to assess air quality during  
177 wildfire events (Lin et al., 2014; Vongruang et al., 2017; Pan et al., 2020). The latest version, FINN v2.5, was introduced in  
178 2022 and incorporates an updated algorithm for determining fire size by aggregating adjacent fire detections. Compared to  
179 FINN1.5, FINN2.5 incorporates significant improvements in input data and processing methods for detecting fire activity,  
180 characterizing annual land use/land cover and vegetation density, estimating burned area, and applying fuel loads across  
181 different global regions (Wiedinmyer et al., 2023). In this study, FINN1.5 and FINN2.5 MOS (MODIS-only fire detections),  
182 and FINN2.5 MOSVIS (MODIS+VIIRS fire detections) were used. Detailed information on emission species and factors can  
183 be found in Tables S2 and S3.

### 184 **2.2.3 GFAS (v1.2)**

185 The GFAS provides data outputs that encompass spatially gridded FRP, DM burning, and BB emissions for numerous chemical,  
186 greenhouse gas, and aerosol species (Andela et al., 2013). These data are globally available from 2003 to the present, with a  
187 regular latitude and longitude grid resolution of 0.1° x 0.1° ([https://ads.atmosphere.copernicus.eu/cdsapp#!/dataset/cams-  
188 global-fire-emissions-gfas](https://ads.atmosphere.copernicus.eu/cdsapp#!/dataset/cams-global-fire-emissions-gfas), last accessed on 11 May 2023). The latest version, GFAS 1.2, includes injection height daily data  
189 (mean altitude of maximum injection and altitude of plume top), which are obtained from the plume rise model and IS4FIRES.  
190 To ensure BB data quality, quality control procedures were applied to the MODIS data. In Figure 2, it is illustrated that GFAS  
191 1.2 data put into the WRF-Chem process, where the missing emission species (Table S4) required for the MOZART-MOSAIC  
192 scheme are added by Jose et al. (2017), Andreae and Merlet (2001), and Andreae (2019) method. Additionally, the mean





193 fraction and fire size of the four vegetation types were obtained from FINN1.5, and the 3-hour time allocation from GFED4.1s  
194 was utilized for the GFAS scheme.

#### 195 **2.2.4 FEER (v1.0-G1.2)**

196 In 2005, a new algorithm was developed by Ichoku and Kaufman (2005) to calculate BB emissions directly from FRP  
197 measurements (<https://feer.gsfc.nasa.gov/data/emissions/>, last accessed on 11 May 2023). This approach aimed to overcome  
198 the delays and uncertainties associated with other variables previously used. Subsequently, their work resulted in the release  
199 of the FEER Ce v1.0 product, a global BB inventory with a resolution of  $0.1^\circ \times 0.1^\circ$ . In this study, the FEERv1.0-G1.2 product  
200 utilizes the GFASv1.2 FRP dataset to provide daily data from 2003 to the present at a spatial resolution of  $0.1^\circ \times 0.1^\circ$ . It  
201 includes species such as CO, SO<sub>2</sub>, NH<sub>3</sub>, NO<sub>2</sub>, OC, BC, PM<sub>2.5</sub>, NMHCs, among others. Notably, the GFASv1.2 dataset has also  
202 been incorporated to ensure compatibility with the MOZART-MOSAIC scheme, as depicted in Table S5.

#### 203 **2.2.5 QFED (v2.5r1)**

204 QFED emissions are estimated using the FRP method and draw on the cloud correction technique developed in the GFAS.  
205 However, QFED employs a more sophisticated approach for non-observed land areas, such as those obscured by clouds (Koster  
206 et al., 2015). Fire locations and FRPs are derived from MODIS Level 2 fire products (MOD14 and MYD14) and MODIS  
207 geolocation products (MOD03 and MYD03). QFEDv2.5r1, covering the period from 2000 to 2023, provides daily average  
208 emissions at a horizontal spatial resolution of  $0.1^\circ \times 0.1^\circ$ , encompassing information on OC, BC, SO<sub>2</sub>, CO, PM<sub>2.5</sub>, and other  
209 species. It can be accessed from <https://portal.nccs.nasa.gov/datashare/iesa/aerosol/emissions/QFED/v2.5r1/> (last accessed on  
210 11 May 2023). Figure 2 shows the detailed process of QFEDv2.5r1 to ensure consistency with the MOZART-MOSAIC  
211 program. Table S5 illustrates the addition of missing data.

#### 212 **2.2.6 IS4FIRES (v2.0)**

213 IS4FIRES is based on a reanalysis of FRP data obtained from the MODIS on the Aqua and Terra satellites. The dataset covers  
214 the period from 2000 to the present (Sofiev et al., 2009). IS4FIRESv2 emissions are global, with a spatial resolution of  $0.1^\circ \times$   
215  $0.1^\circ$ , provided every 3 hours, and represented in five stacked vertical layers (<http://silam.fmi.fi/thredds/catalog/i4f20emis-arch/catalog.html>, last accessed on 11 May 2023) (Soares et al., 2015). It distinguishes between seven vegetation classes:  
216 boreal, temperate, tropical forests, residual crops, grasses, shrubs, and peat. The linear relationship between FRP and PM is  
217 based on the IS4FIRESv1 EF but scaled to vegetation class types using the BB EF described in Akagi et al. (2011). Additional  
218 IS4FIRES emission species according to Jose et al. (2017), Andreae and Merlet (2001) and Andreae (2019), Baró et al. (2021),  
219 and Wiedinmyer et al. (2011) meet the WRF-Chem selected MOZART-MOSAIC scheme (Table S5). It is noteworthy that its  
220 time allocation is processed using the self-contained 3 hours (Figure 2).  
221



## 222 2.3 Observations and Reanalysis Data

### 223 2.3.1 Satellite observations

224 Remote sensing satellite observation is widely utilized to evaluate AOPs, as it offers several advantages (Palacios-Peña et al.,  
225 2018), including non-interference with observed samples, sensitivity to various properties, particularly AOPs relevant to  
226 wildfires, and the ability to provide different types of data products such as points, columns, or profiles (Reid et al., 2013). To  
227 assess the AOD of European wildfires simulated by WRF-Chem, Palacios-Peña et al. (2018) compared products from different  
228 satellite inversions of AOD and selected the best product for model evaluation. Following a similar research approach, we  
229 chose the following satellite products: MODIS, VIIRS, and Himawari-8. In addition, Cloud-Aerosol Lidar and Infrared  
230 Pathfinder Satellite Observation (CALIPSO) satellites were selected to evaluate AEC simulated by WRF-Chem with BB  
231 emissions. Detailed descriptions of various satellite parameters and algorithms can be found in a previous study (Ma et al.,  
232 2021).

233 For a comprehensive understanding of absorbing aerosols emitted by global/regional wildfires, the Tropospheric Monitoring  
234 Instrument (TROPOMI) on the Sentinel-5 Precursor (S5P) satellite, launched on October 13, 2017, was employed to assess  
235 AAOD (Torres et al., 2020; Filonchik et al., 2022). TROPOMI is a high spectral resolution spectrometer that covers the  
236 ultraviolet (UV) to shortwave infrared regions in eight spectral windows, offering enhanced capabilities for atmospheric  
237 monitoring compared to OMI satellites (Veeffkind et al., 2012). Operating in a push-broom configuration, TROPOMI provides  
238 a wide swath width of approximately 2600 km over the Earth's surface. The instrument boasts higher spatial resolution, wider  
239 observation range, increased sensitivity and accuracy, more measurement parameters, and higher temporal resolution, making  
240 it an advanced tool for atmospheric monitoring. The TROPOMI aerosol algorithm (TropOMAER), employed for atmospheric  
241 observations, uses observations at two near-UV wavelengths to calculate UV Aerosol Index (UVAI) and retrieve total column  
242 AAOD and SSA (Torres et al., 2020). The AOD retrieved using TropOMAER inversion on land exhibits a root-mean-square  
243 error (RMSE) comparable to the OMI retrieval (maximum 0.1 or 30%). The RMSE of AOD over water may be two times  
244 larger, while the RMSE of AAOD is estimated to be approximately 0.01 (Torres et al., 2020). For this study, the TropOMAER  
245 L2 product (<https://search.earthdata.nasa.gov/>, last accessed on 11 May 2023) with a spatial resolution of 7.5 km x 3 km was  
246 selected. The WRF-Chem simulated AAOD at 500 nm was derived based on the method proposed by Hu et al. (2016), utilizing  
247 SSA (500 nm) from TROPOMI and Equation (1), where  $\lambda$  represents the wavelength. The uncertainty in SSA is approximately  
248 0.03 (Dubovik and King, 2000)

$$249 \quad \text{AAOD}(\lambda) = [1 - \text{SSA}(\lambda)] \times \text{AOD}(\lambda) \quad (1)$$





### 250 **2.3.2 In-situ observations**

251 To assess the effect of AOPs during wildfires, Baro et al. (2017) and Lin et al. (2014) first validated the meteorological field  
252 and pollutants simulated by WRF-Chem. Therefore, in this study, the FINN 1.5 scheme (the most common scheme used by  
253 WRF-Chem) was selected for validation of the model output for meteorological parameters and pollutants. The selected  
254 meteorological parameters include 2 m temperature (T2), 2 m relative humidity (RH2), and 10 m wind speed (WS10). These  
255 data were obtained from the data-sharing website (<https://rp5.ru/>, last accessed on 11 May 2023) and their global weather  
256 station identifications can be found in Table S6. The PM<sub>2.5</sub> data used to assess the stability of the model were collected from  
257 multiple publicly available website datasets from China (<https://quotsoft.net/air/>, last accessed on 11 May 2023), Thailand  
258 (<http://air4thai.pcd.go.th/webV2/history/>, last accessed on 11 May 2023), and global public datasets ([https://aqicn.org/data-](https://aqicn.org/data-platform/covid19/)  
259 [platform/covid19/](https://aqicn.org/data-platform/covid19/), last accessed on 11 May 2023), and their locations are shown in Table S7.

260 The AERONET (AErosol RObotic NETwork) project is a collaboration between NASA and PHOTONS (PHOtométrie pour  
261 le Traitement Opérationnel de Normalisation Satellitaire; Univ. of Lille 1, CNES, and CNRS-INSU), establishes a  
262 collaborative network involving ground-based remotely sensed aerosol networks. This project has been in existence for over  
263 25 years and provides a long-term, continuous, and easily accessible public-domain database for aerosol research, including  
264 the optical, microphysical, and radiometric properties of aerosols. AOD and AAOD measurements from AERONET are based  
265 on multiple wavelength bands, including visible and near-infrared spectra. Common band ranges include 340 nm, 380 nm, 440  
266 nm, 500 nm, 675 nm, 870 nm, etc. AOD and AAOD data are classified into three levels based on data quality: level 1.0  
267 (unscreened), level 1.5 (cloud shielding and quality control), and level 2.0 (quality assurance). For this study, data at the 2.0  
268 level were used, indicating that the data underwent cloud screening and quality assurance following the detailed procedures  
269 outlined by Smirnov et al. (2000). In the absence of cloud contamination, the uncertainty in AOD was estimated to be 0.01 to  
270 0.02, depending on wavelength. AAOD was calculated using Equation (1).

### 271 **2.3.3 ERA5 Reanalysis data**

272 European Centre for Medium-Range Weather Forecasts (ECMWF) Reanalysis v5 (ERA5) is a global meteorological reanalysis  
273 dataset developed and maintained by the ECMWF (Hersbach et al., 2018). The ERA5 dataset is based on global observational  
274 data, satellite remote sensing data, and numerical model forecast data. It uses advanced data assimilation techniques to fuse  
275 data from these different sources to produce consistent and high-quality global meteorological reanalysis data. Hourly data are  
276 available from 1979 up to the current time, and ERA5 data have a spatial resolution of 0.25° x 0.25° (about 25 km) at the  
277 horizontal level. In this paper, the effect of ERA5 950 hpa wind on BB aerosols is analyzed.

### 278 **2.4 Methodology**

279 In order to assess AOD, AAOD, AEC, and DRF using WRF-Chem with different BB inventories, apart from the FINN schemes,  
280 other emissions inventories are re-gridded and time-allocated, as shown in Figure 2. Subsequently, species are supplemented



281 according to the gas-phase chemistry and aerosol scheme (MOZART-MOSAIC) employed by WRF-Chem. It is worth noting  
282 that all scenarios utilized fire size and vegetation type proportion data from FINN1.5 to calculate smoke plume rise. The  
283 performance of WRF-Chem model simulations against measurements is evaluated using statistical metrics (Wu et al., 2019)  
284 including the mean bias (MB), RMSE, Correlation coefficient (R), and the index of agreement (IOA) in Table S8. This research  
285 further investigated DRF over PSEA during the study period. Zhao et al. (2013) and Lin et al. (2014) were referenced for the  
286 treatment of BB aerosol radiative forcing, as shown in the following equations.

$$\text{DRF} = (F_i^\downarrow - F_i^\uparrow) - (F_{no-fire}^\downarrow - F_{no-fire}^\uparrow) \quad (2)$$

287 where  $F^\uparrow$  and  $F^\downarrow$  indicate the aerosol upward radiation flux and the aerosol downward radiation flux, respectively.  $i$  indicates  
288 that WRF-chem is added to the different BB emission inventories, and *no-fire* denoted scene without BB inventory applied.

## 289 3 Result

### 290 3.1 Inter-comparison of Eight BB Inventories.

291 Several studies have utilized OC as a measurable metric to compare variations among multiple BB inventories (Reddington et  
292 al., 2016; Carter et al., 2020). This is because OC is a major component in smoke particles from fresh BB, with mass fractions  
293 ranging from 37% to 67% depending on the fuel type (Pan et al., 2020). Figure 3 presents the spatial distribution characteristics  
294 of OC for the eight BB datasets in the study region, along with the total OC emissions in the PSEA region during March 2019.  
295 The highest OC emissions across all datasets are observed in the northern regions of Laos, Cambodia, and Thailand, as well  
296 as in eastern and western Myanmar and southern Bangladesh. Lower emissions are observed in the central regions of Myanmar  
297 and Thailand, northern Vietnam, and southern regions of China. Similar spatial distribution characteristics of OC emissions in  
298 the PSEA region during March have also been reported by Pan et al. (2020) and Reddington et al. (2021). These emissions  
299 mainly originate from shrubland, evergreen broadleaf, mixed shrubland/grassland, and dryland cropland, as classified by the  
300 WRF-Chem land use data in the PSEA (Figure S1). The eight BB emissions, ranked based on their total OC emissions (PSEA)  
301 in descending order, are FINN2.5 MOSVIS (2.533 Tg/M), FINN2.5 MOS (2.002 Tg/M), QFED (1.303 Tg/M), FINN1.5 (1.214  
302 Tg/M), IS4FIRES (0.604 Tg/M), FEER (0.462 Tg/M), GFAS (0.296 Tg/M), and GFED (0.295 Tg/M). The highest OC  
303 emission in the dataset is exhibited by FINN2.5 MOSVIS, which can be attributed to the use of updated burned area data and  
304 the inclusion of fire information from VIIRS, capturing a larger number of small-scale fires (Wiedinmyer et al., 2023). The  
305 lowest OC emissions are provided by GFED, which may have underestimated DM and agricultural fire EF (OC, EF=2.3 g/kg),  
306 and GFAS, which only underestimated DM. The overall mean and standard deviation of OC for different BB emission  
307 inventories in the PSEA region was  $1.09 \pm 0.83$  Tg/M, with a coefficient of variation (CV) of 76% (CV is defined as the ratio  
308 of the standard deviation to the mean of all inventories).

309 Figure 4 illustrates the total emissions of the eight emission inventories in the PSEA region during March 2019 added to the  
310 WRF-Chem after processing (Figure 2). It also presents the percentage composition of CO, OVOCs, NMHCs, NO<sub>x</sub>, Gas (SO<sub>2</sub>



311 and  $\text{NH}_3$ ),  $\text{PM}_{2.5}$ ,  $\text{PM}_{10}$ , BC, and OC. The total BB emissions (aerosol and gas) are ranked as FINN2.5 MOSVIS (105.7 Tg/M),  
312 FINN2.5 MOS (83.7 Tg/M), FINN1.5 (41.9 Tg/M), IS4FIRES (19.4 Tg/M), FEER (15.4 Tg/M), QFED (11.1 Tg/M), GFED  
313 (10.3 Tg/M), and GFAS (9.9 Tg/M). Although the total QFED emissions are low, the aerosol emissions (OC, BC,  $\text{PM}_{2.5}$ ,  $\text{PM}_{10}$ )  
314 are not, just smaller than the FINN schemes. The PSEA aerosol emissions from FINN2.5 are higher than those predicted for  
315 FINN1.5 and approximately twice as high as the latter, consistent with the findings of Wiedinmyer et al. (2023). Among them,  
316 the highest and lowest emissions of OC+BC are observed in FINN2.5 MOSVIS (2.82 Tg/M) and GFAS (0.32 Tg/M),  
317 respectively. Since the FINN schemes employ the EF from Akagi et al. (2011) and subsequent updates, the proportions of each  
318 species are relatively similar. In summary, FINN schemes (v1.5 and 2.5) have relatively high total aerosol emissions compared  
319 to the other schemes, and the "top-down" scenario (GFAS, FEER, QFED, IS4FIRES) does not have high total emissions  
320 despite being constrained by the AOD. To evaluate the spatiotemporal distribution characteristics of absorbing aerosols from  
321 BB emissions, particularly the BC to OC ratio, was also displayed in Figure 4. Except for QFED, which exhibits a lower ratio  
322 of approximately 0.08 (1/13), the ratios for the other BB datasets are greater than or equal to 0.1(1/10).

### 323 **3.2 Model Validation**

324 To assess the AOPs and DRF simulated by the WRF-Chem adding different BB emissions, the stability of the model is verified  
325 by comparing the simulated meteorological fields and  $\text{PM}_{2.5}$  concentrations with observations at monitoring stations using the  
326 WRF-Chem with the FINN1.5 scheme. The statistical results in Table S6 demonstrate good agreement ( $\text{IOA} \geq 0.6$ ) between  
327 the simulated T2, RH2, and WS10 and the data from 13 stations. However, at some stations, the wind speed RMSE exceeds 2  
328 m/s, which may be attributed to unresolved topographic features in the surface drag parameterization (Saide et al., 2016). The  
329 bias between observations and simulations for RH2 can be partially explained by the influence of different surface and  
330 boundary layer parameterizations on the simulated near-surface water vapor fluxes (Chen et al., 2019). During the wildfire  
331 period of March 2019, the daily average observed  $\text{PM}_{2.5}$  concentrations of 23 cities at the surface were compared with the  
332 model results for the FINN1.5 case in Figure S2, where the statistical indicators are shown in Table S7. The WRF-Chem was  
333 able to simulate  $\text{PM}_{2.5}$  concentrations in urban sites located in the high BB emission region of northern Laos (Chiang Rai  
334 Mueang in northern Thailand and Jinghong in China) with consistency to the observed data (R of 0.64 and 0.75, respectively),  
335 where the model was able to reproduce the pollution peaks (IOA of 0.74 and 0.82, respectively). In a previous study by  
336 Vongruang et al. (2017), the WRF-CMAQ model was used to simulate  $\text{PM}_{2.5}$  in the PSEA region by incorporating BB  
337 emissions (GFAS v1.1 or FINN1.5) and comparing them with observed stations. The average IOA value was 0.51 (with the  
338 optimal IOA being 0.69). In this study, all 23 stations had IOA values greater than 0.51 (with over 52% exceeding 0.69),  
339 indicating that the model can consistently reproduce the spatial and temporal distribution characteristics of pollutants in the  
340 PSEA region. Although the WRF-Chem model could reasonably capture the spatial-temporal characteristics of  $\text{PM}_{2.5}$   
341 concentrations observed in most cities ( $\text{IOA} > 0.54$ ), the influence of anthropogenic emission inventories and BB vertical  
342 transport may lead to biases in some areas (e.g., Hong Kong).



### 343 3.3 AOD

#### 344 3.3.1 Satellites vs. AERONET AOD

345 The linear regression results between AOD daily averages from different satellite sensors and AERONET data are shown in  
346 Figure S3. Overall, during the wildfire event in the PSEA region, the DB algorithm of VIIRS demonstrated the best skill, as  
347 indicated by optimal  $R^2$  and RMSE values. Su et al. (2022) found that VIIRS DB also exhibited the highest accuracy and  
348 stability when analyzing long-term multiple satellite inversions of AOD aerosol datasets in Asia. This is because VIIRS DB  
349 incorporates upgraded surface and aerosol models specifically designed for Asian regions, which have not been applied to the  
350 MODIS DB (Sayer et al., 2019). Therefore, to evaluate the representation of AOD in the WRF-Chem experiments for the  
351 PSEA wildfires in March 2019, the AOD at 550 nm provided by VIIRS DB (along with AERONET observations) was chosen  
352 to determine biases and errors in the conducted experiments.

#### 353 3.3.2 WRF-Chem vs. VIIRS AOD

354 To assess the agreement between the simulated AOD from WRF-Chem and the observed AOD, we utilized the extracted data  
355 (WRF-Chem) based on VIIRS satellite transit time and compared the daily average values with AERONET observations.  
356 Figure 5 illustrates the daily average AOD at 550 nm from the VIIRS and wind (scaled in 10 m/s) at 900 hPa (a), along with  
357 the corresponding AOD from the WRF-Chem simulation over the PSEA region during March 2019, considering different BB  
358 scenarios (b-i). The high AOD (HAOD,  $AOD > 1.0$ ) derived from VIIRS retrievals is primarily concentrated in Laos, Thailand,  
359 and Vietnam (97-110°E, 15-22.5°N). Additionally, Beibu Gulf and coastal cities in southern China also exhibit high AOD  
360 values ( $AOD > 0.6$ ), which may be attributed to the long-range BB transport of tropical westerly and southwesterly winds  
361 depicted in Figure 5(a). The FINN (v1.5 and 2.5), FEER, QFED, and IS4FIRES schemes demonstrate the ability to reproduce  
362 high aerosol concentrations in areas with elevated AOD values as observed by VIIRS satellites. These simulations align with  
363 the spatial distribution of monthly mean AOD during the wildfire period in the PSEA simulations conducted by Dong and Fu  
364 (2015b). However, the GFED and GFAS schemes fail to capture the high AOD areas in the PSEA region, likely due to the  
365 low BB emission inventories of the input model (Pan et al., 2020).

366 Figure 6 ((a)-1 to (a)-8) displays the estimated MB between the model with eight BB scenarios and VIIRS daily mean AOD.  
367 The FINN schemes (v1.5 and 2.5) noticeably overestimate AOD in the HAOD region, while the GFED, GFAS, FEER, and  
368 IS4FIRES schemes underestimate AOD. Moreover, the FINN schemes also exhibit AOD overestimation in the Beibu Gulf,  
369 South China Sea, Bay of Bengal, and Andaman Sea. As the FINN schemes have the largest aerosol emissions compared to  
370 other BB emissions (Figure 4), it may lead to an overestimation of AOD in the HAOD region. All schemes exhibit varying  
371 degrees of overestimation for a significant portion of southern China. Table 2 provides statistics on the MB of AOD between  
372 satellite-retrieved and WRF-Chem AOD in the HAOD region. The AOD simulated by FINN schemes are significantly  
373 overestimated, whereas the rest of the schemes exhibit underestimation. Although FEER (-0.12) and IS4FIRE (-0.14)  
374 underestimate the simulated AOD, their performance is considerably better than other BB emission inventories. As highlighted



375 by Palacios-Pena et al. (2017) and Crippa et al. (2019), the MB between simulated and observed AOD can be attributed to  
376 estimation errors in BB uncertainty, aerosol dry mass, and specifically related to the certain mass of small particles or too  
377 much moisture associated with the aerosol. The RMSE estimation (Figure 6(b)-1 to (b)-8) reveals noticeable uncertainty in the  
378 FINN schemes compared to other schemes in the HAOD and southern China, while the performance of the remaining schemes  
379 in simulating AOD in Laos and northern Thailand is unsatisfactory. The RMSE statistics in Table 2 show that the AOD  
380 simulated by the FINN2.5 schemes (MOS and MOSVIS) have greater uncertainty in the HAOD region compared to FINN1.5,  
381 and the RMSE of the other schemes are generally comparable. Figure 6(c)-1 to (c)-8 depicts the temporal R between simulated  
382 AOD and observations, with high values of R ( $>0.6$ ) concentrated in Laos and northern Thailand, Myanmar, the Bay of Bengal,  
383 the Andaman Sea, and the South China Sea. The FINN2.5 MOSVIS scheme exhibits the highest R compared to other schemes  
384 in the HAOD region (Table 2), potentially due to the updated acquisition time (local time) and increased VIIRS data, leading  
385 to improved R with the observed data.

### 386 3.3.3 WRF-Chem vs. AERONET AOD

387 Figure 7 illustrates the time series of AOD at 550 nm, measured at the 16 AERONET sites marked in Figure 1, in comparison  
388 to simulated AOD from WRF-Chem with different BB emissions. These 16 sites are categorized into three major classes,  
389 namely, the satellite inversion of HAOD regions (97-110°E, 15-22.5°N, Figure 7 a-g), the adjacent HAOD area (AHAOD,  
390 Figure 7 h-l), and the downwind area (DA, Figure 7 m-p), allowing for further analysis of AOD variations during wildfire  
391 events. In the HAOD stations (Laos, Chiang Mai, Fang, Nong Khai, Son La, and Ubon Ratchathani), high aerosol loading was  
392 captured by all schemes and AERONET sites on March 15, 23, and 30, respectively. Among the sites, the Laos station  
393 performed the best in terms of simulated and observed AOD mean R and IOA for all BB scenarios, with R and IOA values of  
394 0.82 and 0.80, respectively (Table 3). To compare the performance of the multi-BB emission scenario model for the AOD  
395 simulation, a Taylor diagram was constructed (Figure 8). The Taylor diagram demonstrates that, in the HAOD regions, the  
396 FINN schemes (v1.5 and 2.5) exhibit a higher overall R compared to other schemes when simulating AOD against observations.  
397 Furthermore, the FINN2.5 schemes show a slightly better correlation than FINN1.5. Among the eight schemes, the IS4FIRES  
398 and FINN1.5 schemes simulated AOD performed better in terms of consistency and deviation from the observed comparison  
399 in the HAOD region (Figure 8(a)). In the AHAOD stations, peaks of AOD simulated by WRF-Chem were also found on three  
400 dates (March 15, 23, and 30), but these peaks were lower than the HAOD in Figure 7. Despite the FINN2.5 MOSVIS scheme  
401 showing the best correlation between simulated AOD and observations in the HAOD regions compared to other schemes, its  
402 performance in AHAOD regions was unsatisfactory (Table 3). Poorly performing stations in the AHAOD regions included  
403 Bangkok, Silpakorn, and Songkhla, which are located between 0° and 22.5° N latitude (Figure 7). This discrepancy may be  
404 attributed to the assumptions made by the FINN2.5 MOSVIS scheme for fire detection in the equatorial region to achieve daily  
405 global coverage (Wiedinmyer et al., 2023) and the overestimation of AOD values by WRF-Chem, which can be explained by  
406 the presence of excess aerosol dry mass (Chapman et al., 2009). In the DA regions, such as Hong Kong and Taiwan, high



407 concentrations of aerosols were simulated and observed after March 23 in Figure 7. Previously, studied the same event using  
408 models and ground measurements and reported a contribution of BB of about 56% to local AOD and 26%-62% to DA.

### 409 **3.4 AAOD**

#### 410 **3.4.1 WRF-Chem vs. TROPOMI AAOD**

411 Wildfire releases significant amounts of absorbing aerosols such as OC and BC, which can absorb solar radiation and increase  
412 the radiation absorption capacity of the atmosphere, thereby affecting the Earth's radiation balance. Therefore, it is crucial to  
413 evaluate the model's ability to simulate absorbing aerosols using AAOD results obtained from satellite observations. To reduce  
414 the discrepancies caused by missing data in the inversion of different observations, the WRF-Chem simulations are matched  
415 with the observed data. Figure 9 shows the spatial distribution of daily mean AAOD at 500 nm retrieved by TROPOMI (a)  
416 and simulated by WRF-Chem with eight BB emissions (b-j) during March 2019 in the PSEA region. The high AAOD (AAOD >  
417 0.03) from TROPOMI is mainly concentrated in northern Laos, northern Vietnam and northern Thailand, and eastern Vietnam,  
418 which is similar to the spatial distribution characteristics of HAOD provided by VIIRS. Kang et al. (2017) also found similar  
419 AAOD distribution patterns when studying the spatial and temporal characteristics of absorbing aerosols in Southeast Asia  
420 from 2005 to 2016. The WRF-Chem simulations with different BB emissions exhibit high AAOD values not only in the  
421 aforementioned regions but also in southern China and the South China Sea (Figure 9). Figure 10 shows the spatial distribution  
422 characteristics of MB(a), RMSE(b), and R(c) for the comparison of TROPOMI-inverted AAOD with WRF-Chem-simulated  
423 AAOD using different BB scenarios. All FINN, FEER, and IS4FIRES schemes overestimate AAOD in the HAOD region (97-  
424 110°E, 15-22.5°N) compared to TROPOMI inversion, with FINN2.5 showing the most significant overestimation (Figure  
425 10(a)-1 to (a)-8). Table 2 further confirms these overestimations with statistics of 0.056, 0.073, 0.08, 0.02, and 0.018,  
426 respectively. The overestimation may arise from underestimating AAOD in TROPOMI, as well as overestimating absorbing  
427 aerosols in the BB inventory and uncertainties in the representation of absorbing aerosols by WRF-Chem, including aerosol  
428 size distribution, chemical composition, aging processes, vertical and horizontal transport (including injection heights for fire  
429 emissions), and errors in dry/wet removal from the atmosphere. Figure 10(b)-1 to (b)-8 and Table 2 demonstrate that the FINN  
430 schemes exhibit greater uncertainties in simulating AAOD in the HAOD region compared to other schemes. Comparing the R  
431 between satellite-retrieved AAOD and simulated AAOD, values of  $R > 0.6$  are primarily concentrated in northern Laos,  
432 northern Thailand, and Myanmar. Particularly, the FINN2.5 MOSVIS scheme, due to the incorporation of improved local time  
433 and inclusion of small fires from VIIRS, exhibits the best correlation with the simulated AAOD relative to satellite retrievals  
434 (Table 2).

#### 435 **3.4.2 WRF-Chem vs. AERONET AAOD**

436 To reduce the uncertainty caused by missing AERONET data, quality control has been applied to the AERONET site data  
437 (samples > 10 days). In the HAOD region within the range of 97-110°E, 15-22.5°N, where both the satellite-retrieved AOD





438 and AAOD exceed the thresholds of 1 and 0.03 (BB high emission area), respectively. Figure 11 presents a comparison of  
439 time series between AAOD measurements from four AERONET sites within the HAOD region and AAOD simulated by the  
440 nearest corresponding AERONET site using WRF-Chem with different BB inventories. Similar to peaks of AOD, AAOD  
441 from the Doi Ang Khang site also exhibits peaks on March 15th, 23rd, and 30th. Although most schemes can capture the high  
442 AAOD loading, the performances of the GFED, GFAS, and QFED schemes are unsatisfactory (Table S9). This could be  
443 attributed to lower concentrations of absorbing aerosols or inaccurate spatial distribution in the BB emission inventories  
444 (Reddington et al., 2016). The Fang site shows the best mean R and IOA among the eight BB scenarios simulating AAOD  
445 compared with AERONET, with R and IOA values of 0.69 (Table S9). The Taylor diagram indicates that the FINN schemes  
446 perform better than others in representing AAOD in Figure 8 (b), which may be the FINN schemes for unique calculating  
447 biomass burned area and EF that are more suitable for the HAOD region (Wiedinmyer et al., 2011; 2023). When comparing  
448 simulated AAOD with observations for the FINN2.5 MOSVIS scheme, both the R and IOA perform better than other schemes  
449 at all sites. The improved performance of the FINN2.5 MOSVIS scheme in simulating AAOD during wildfires in the PSEA  
450 region can be attributed to two factors: the inclusion of smaller fires using VIIRS 375m fire detection data and updated  
451 information on time and burned area.

### 452 **3.5 AEC**

453 Although AOD and AAOD provide useful information about atmospheric aerosol loading, there is limited information  
454 available regarding the vertical distribution of aerosols. Palacios-Peña et al. (2018) found that uncertainty in the vertical  
455 distribution of aerosols during wildfires in Europe affects AOPs. The CALIPSO, with its unique capability to actively retrieve  
456 vertical aerosol spatial distribution, offers an opportunity to assess the simulation of aerosol vertical optical properties by  
457 WRF-Chem during wildfire events. Figure 12 displays the aerosol vertical extinction profiles at 532 nm retrieved by CALIPSO  
458 in the HAOD region during March 2019, along with the aerosol extinction profiles (550 nm) simulated by various BB schemes,  
459 where model data are matched with CALIPSO overpass times. AEC retrieval by CALIPSO is greater than 0.2 within the range  
460 of 0.5 km to 4 km above ground level, possibly due to the uplifted aerosols from wildfires. WRF-Chem utilizes the smoke  
461 plume rise model, with upper and lower limits of heat flux determined for each land type, to calculate the minimum and  
462 maximum plume heights, and the emitted pollutants are distributed across each vertical layer within the injection height (Grell  
463 et al., 2011). From 0.5 km to 4 km, the trends of AEC changes in the eight BB schemes are consistent with CALIPSO,  
464 indicating that the employed smoke plume rise model in WRF-Chem can reproduce the minimum and maximum plume heights.  
465 However, all the FINN schemes overestimate AEC compared to CALIPSO from 0.5 km to 4 km, while the other schemes  
466 underestimate it. The aerosol concentration in the BB emission inventories may play a decisive role, leading to differences in  
467 the AEC (Reddington et al., 2019). At 4-8 km, the AEC gradually tends to zero with increasing altitude, while the AEC from  
468 the CALIPSO still has three peaks, which may be due to the uncertainty of the model for the BB injection height calculation  
469 or the effect of external dust transmission (Dong and Fu, 2015a; Jin et al., 2022).



### 470 **3.6 DRF**

471 Considering the significant impact of BB aerosols on radiation, this study investigates the radiative perturbation of SW  
472 radiation caused by BB aerosols under clear-sky conditions at the top of the atmosphere (TOA), surface (SFC), and in the  
473 atmosphere (ATM). The focus is on the DRF of BB aerosols during the daytime, as Ge et al. (2014) found that local  
474 convergence in the smoke source region caused by smoke during the daytime transmits more smoke particles on the above  
475 surface. Figure 13 illustrates the spatial distribution of daytime average SW radiative perturbation caused by BB aerosols  
476 during 2019 March in the PSEA region at the TOA, ATM, and SFC. It is evident that BB aerosol DRF exists not only in the  
477 PSEA region but also in other regions such as southern China, Hong Kong, and Taiwan. The spatial distribution of SW radiative  
478 perturbation by BB aerosols aligns with the simulated distribution of AOD, with the highest values observed in the HAOD  
479 region (97-110°E, 15-22.5°N). Lin et al. (2014) have confirmed that BB aerosols, mainly BC and OC, play significant roles in  
480 the radiative budget. On one hand, the solar absorption by BC in the atmosphere increases the rate of radiative heating, leading  
481 to a significant decrease in solar radiation reaching the surface. On the other hand, OC enhances the reflected solar radiation  
482 at the TOA, resulting in a cooling effect due to reduced incident solar radiation on the atmosphere and surface. The SW  
483 radiative perturbation of BB in TOA is negative with a cooling effect in the model domain for eight scenarios, except for areas  
484 with high surface albedo such as Himalayan glaciers. Figure 14 shows that during the wildfire period in the HAOD region, the  
485 eight schemes exhibit DRF of  $-30.89 \pm 23.6 \text{ W/m}^2$  at TOA. The SW radiative perturbation of BB aerosol at TOA depends  
486 largely on the SW absorption rate of BB aerosol. The FINN schemes (v1.5 and 2.5) exhibit a significantly stronger cooling  
487 effect compared to other schemes, possibly due to higher BC concentrations in BB emissions compared to other inventories.  
488 At the ATM, the absorption by BB aerosols leads to a positive radiative forcing, causing atmospheric warming, particularly in  
489 the HAOD region. In the HAOD region, the eight schemes exhibit a BB aerosol SW DRF of  $1.70 \pm 1.40 \text{ W/m}^2$  in the ATM  
490 (Figure 14). WRF-Chem can simulate the heating effect of BB aerosols in the ATM regardless of the BC/OC ratio used in the  
491 emission inventory (1:8, 1:9, or 1:13). At the SFC, the cooling effect is due to the scattering of non-absorbing atmospheric  
492 aerosols and absorbing aerosols that increase the radiative heating rate, resulting in a significant reduction of solar radiation  
493 reaching the surface. The eight schemes simulate the DRF of  $-32.60 \pm 24.50 \text{ W/m}^2$  at SFC in the daytime (with FINN2.5  
494 MOSVIS reaching a maximum of  $70 \text{ W/m}^2$ ), which is comparable to the level of the PSEA region studied previously by Lin  
495 et al. (2014) and Ge et al. (2014).

### 496 **4. Discussion**

497 Biases in the simulated AOPs (AOD, AAOD, AEC) over tropical BB have been attributed to a variety of factors (Reddington  
498 et al., 2016), including (1) uncertainties in BB emission fluxes, (2) errors in modeling the atmospheric distribution and  
499 properties of BB aerosols. These deviations in optical properties further affect the DRF, leading to uncertainties in the  
500 assessment of climate change.



#### 501 **4.1 BB Emission Fluxes**

502 Uncertainties associated with the derivation of emission fluxes arise from errors in satellite detection of active fire or burned  
503 areas (e.g., cloud and smoke obscuration of the surface, satellite spatial resolution and detection limitations, and satellite  
504 exceedance times), as well as uncertainties in EF and fuel consumption estimates (Carter et al., 2020; Wiedinmyer et al., 2023).  
505 Eight BB inventories were inverted from MODIS data, but there were significant gaps between the bandwidths of MODIS in  
506 the equatorial region, as well as difficulties in detecting fires located under thick clouds, and a reduction in fire detection  
507 sensitivity at the scan edge sensitivity, leading to an underestimation of total regional BB emissions (Wang et al., 2018). In  
508 this paper, The FINN2.5 dataset (BB emission fluxes and AOPs) is consistently higher than the other datasets, with FINN2.5  
509 MOSVIS being the highest overall. FINN2.5 includes improved burned area calculations, uses year-specific land cover and  
510 vegetation datasets, updates fuel loads and EF, and can use multiple fire detection satellite inputs (e.g., MODIS and VIIRS),  
511 which may account for the improved BB emission fluxes. In the PSEA region, during wildfire events, the BB emissions from  
512 FINNv2.5 are consistently higher than the emissions provided by FINNv1.5, approximately twice as much as the latter, even  
513 when considering only MODIS fire detections. The increase in emissions is primarily attributed to the new treatment of burned  
514 areas (Wiedinmyer et al., 2023). Despite updates to input data, parameters, and processing methods, the FINN2.5 scheme tends  
515 to overestimate AOPs compared to observations. This overestimation may arise from inaccurate ecosystem identification (e.g.,  
516 tropical forests instead of shrublands or areas with fewer trees) and fuel load allocation (Pan et al., 2020). Furthermore, in  
517 tropical regions, the FINN scheme employs smoothing of fire detections to mitigate the impact of clouds, which could lead to  
518 an overestimate of BB emissions (Wiedinmyer et al., 2011; 2023). QFED provides relatively higher OC concentrations, but  
519 lower total BB emissions, and the primary driving factors behind these differences are the assumed fuel types and related EF.  
520 Therefore, it is inappropriate to consider OC as the sole criterion for evaluating BB emission fluxes when comparing multiple  
521 BB emission inventories. Although the aerosol concentrations provided by QFED are larger than those of IS4FIRES and FEER,  
522 the simulated AOPs and DRF of this scheme are lower than those of the latter, which may be due to the influence of secondary  
523 pollutant emission precursors (NO<sub>2</sub>, NH<sub>3</sub>, etc.). Previous studies have often used an expansion of aerosols (BC+OC) in the BB  
524 emission inventories by a factor of 3-6 to assess the AOPs (Reddington et al., 2016; Marlier et al., 2013), and the simulation  
525 results from the QFED scheme above reveal that there may be significant uncertainties in this expanded aerosol (BC+OC)  
526 approach. Although GFED4.1s improves the detection of small fires, the agricultural EF = 2.3 g/kg is lower than in other  
527 emission inventories, which could result in an underestimation of AOPs simulated by WRF-Chem with the GFED scheme.  
528 Yin (2020) found that BB in the PSEA region from 2001 to 2018 was predominantly driven by agro-residue burning and  
529 shrubland fires while GFED4.1s underestimation of DM for both fires and the mismatch in vegetation types may have  
530 contributed to the underestimation of BB emission fluxes (Reddington et al., 2016). In general, FRP-based estimation methods,  
531 such as GFAS, FEER, QFED, and IS4FIRES, allow for a more direct estimation of fuel consumption from fire-release energy  
532 without the uncertainty associated with the estimation. However, in the PSEA region, when the FRP from MODIS inversion



533 is observed at a nominal spatial resolution of 1 km at its nadir, it risks missing a large number of smaller fires, as well as  
534 missing fires that are obscured by clouds (Dong and Fu, 2015b), which may lead to an underestimation of the simulated AOPs.

#### 535 **4.2 Modeling Uncertainty and Calculation Bias**

536 The representation of BB aerosols in the model is inadequate, including insufficient characterization of aerosol size distribution,  
537 chemical composition, aging processes, vertical and horizontal transport (including injection heights of fire emissions), and  
538 model errors in dry/wet deposition from the atmosphere (Palacios-Peña et al., 2018; Reddington et al., 2016). Sensitivity  
539 experiments using the global aerosol model reveal that calculations of hygroscopicity growth are most sensitive in simulating  
540 AOD (Reddington et al., 2016). The contribution of SOA formed through the oxidation of VOCs in BB plumes is also a  
541 significant source of uncertainty (Jathar et al., 2014). In this study, we employed the meteorological chemistry and aerosol  
542 scheme: MOZART-MOSAIC\_4bin\_aqueous, which includes aqueous-phase chemistry and SOA, but this mechanism may  
543 lead to overestimation/underestimation of AOPs in the model. The smoke plume rise model developed by Freitas et al. (2010)  
544 was used to vertically represent smoke plumes. Although all schemes capture the vertical profiles of BB aerosol extinction  
545 from 0.5 km to 4 km altitude, some deviations still exist. Previous research has indicated that assuming all fire emissions  
546 injected at the top of the plume could be a worse assumption than prescribing surface-based emissions, which may lead to  
547 deviations in simulated AOPs (Mallia et al., 2018). The AEC is not characterized in all BB scenario simulations for 4-8 km,  
548 which may also lead to an underestimation of AOD or AAOD, and this high-level perturbation of AEC may come from the  
549 influence of external dust aerosols, so the model emission inventory should consider the effect of dust emissions. Others studies  
550 have also found that uncertainties in anthropogenic emission inventories can also lead to simulation errors in AOPs and DRF  
551 during wildfires in the PSEA region (Dong and Fu, 2015a). Although we used the latest version of EDGAR 2015 data, there  
552 may be some underestimation of such emission inventories with a large number of incoming factories in the PSEA region  
553 (Yang, 2016). Additionally, the inclusion of direct and indirect radiation feedback in the WRF-Chem model has been found to  
554 effectively improve the simulation of AOPs in European wildfire simulations (Palacios-Peña et al., 2019), whereas this study  
555 only incorporates aerosol direct radiative feedback. In the calculation of the AOPs, uncertainties associated with the optical  
556 properties of the assumed BB aerosols, such as their refractive index, may also lead to biases in the AOPs. There is some  
557 uncertainty in the AOD from the VIIRS satellite inversion and in the SSA and AAOD from the TROPOMI inversion due to  
558 cloud cover effects in the PSEA region, which may also lead to biased assessments. In addition, the closest proximity method  
559 used in the gridding process of BB emission inventories can also lead to some calculation errors.

#### 560 **5. Summary and Conclusion**

561 This study conducted sensitivity analyses to simulate AOPs and DRF in the PSEA region using eight commonly global BB  
562 emission inventories (GFED, FINN1.5, FINN2.5 MOS, FINN2.5 MOSVIS, GFAS, FEER, QFED, IS4FIRES) and the WRF-  
563 Chem model. The main findings can be summarized below.



564 Regarding BB emissions in the PSEA region, high OC emissions in all datasets (BB) are mainly concentrated in the northern  
565 parts of Laos, Cambodia, and Thailand, and in eastern Myanmar, with a difference in emissions of about a factor of 9 (0.295-  
566 2.533 Tg/M), an overall mean and standard deviation of  $1.09 \pm 0.83$  Tg/M and a CV of 76%, respectively. Those high BB  
567 emissions are primarily from savanna and agricultural fires. OC emissions in GFED and GFAS are significantly lower than in  
568 the other inventories. This is attributed to lower DM and agricultural fire EF in GFED, while DM is underestimated in GFAS.  
569 The OC in FINN2.5 VISMOS is about twice as high as those in FINN1.5, which is explained by the difference in DM rather  
570 than EF. Total aerosol emissions are relatively high in the FINN scenarios (v1.5 and 2.5) compared to the other scenarios.  
571 Although the "top-down" emission inventories (GFAS, FEER, QFED, IS4FIRES) are constrained by the AOD from MODIS,  
572 the total aerosol emission flux is still insufficient.

573 The AOD from VIIRS (DB algorithm) demonstrates the best ability to retrieve the AOD compared to AERONET data. An  
574 evaluation of the AOPs in the PSEA region during March 2019 reveals different performances between observations (VIIRS,  
575 TROPOMI, AERONET) and BB emission inventories. When comparing the AOD simulated by WRF-Chem with the observed  
576 AOD from VIIRS, the FINN1.5, FEER, QFED, and IS4FIRES schemes show a better ability to reproduce high aerosol  
577 concentrations in the HAOD region, the GFED and GFAS schemes show limitations in characterizing these regions. The FINN  
578 (v1.5 and 2.5) schemes tend to overestimate AOD in the region, while other schemes underestimate AOD. The comparison  
579 with AERONET data further highlights the performance of different BB emission scenarios, with the FINN1.5 and IS4FIRES  
580 scenarios generally showing better agreement with observations. For AAOD comparison, it was found that the WRF-Chem  
581 simulations with different BB scenarios were less capable of simulating AAOD than AOD. The unsatisfactory performance of  
582 the GFED, GFAS, and QFED schemes may be due to low concentrations of absorbing aerosols or inaccuracies in the spatial  
583 distribution of BB emissions. Among the evaluated BB scenarios, the FINN1.5 schemes generally performed better in  
584 representing AAOD. Particularly, the FINN2.5 MOSVIS scheme, due to the incorporation of improved local time and inclusion  
585 of small fires from VIIRS, exhibits the best R with the simulated AOD and AAOD relative to observations. CALIPSO  
586 observations versus AEC simulated by WRF-Chem suggest that the smoke plume rise model can reproduce the minimum and  
587 maximum smoke plume heights of wildfire aerosols. However, the FINN (v1.5 and 2.5) schemes tend to overestimate the AEC  
588 compared to CALIPSO, while the other scenarios underestimate it. Regarding the DRF, the spatial distribution of the SW  
589 radiative disturbances due to BB aerosols closely follows the pattern of the AOD. the FINN (v1.5 and 2.5) schemes exhibit a  
590 stronger cooling effect at TOA, which may be due to the higher BC concentration in its emissions. In the HAOD region, BB  
591 aerosols exhibited a daytime SW radiative forcing of  $-32.60 \pm 24.50$  W/m<sup>2</sup> at the SFC, positive forcing ( $1.70 \pm 1.40$  W/m<sup>2</sup>) in the  
592 ATM, and negative forcing ( $-30.89 \pm 23.6$  W/m<sup>2</sup>) at the TOA. Overall, the FINN scenarios (especially FINN2.5) result in an  
593 overestimation of the AOPs in the PSEA region due to an overestimation of DM rather than EF, which in turn may lead to an  
594 overestimation of the DRF. Although the FINN2.5 MOSVIS scenario presents an overestimation of AOPs, the R is the best.  
595 Although the "top-down" emission inventory (GFAS, FEER, QFED, IS4FIRES) is constrained by the AOD from MODIS, the  
596 total aerosol emission flux is still insufficient, which leads to an underestimation of the AOPs modeled by WRF-Chem in the  
597 PSEA region. In addition, uncertainties in anthropogenic emissions, dust emissions, and vertical distribution of aerosol



598 concentrations, may be attributed to differences from simulations versus observations during the wildfire period in the PSEA  
599 region.

600 Additional evaluations of satellite-based fire emission inventories, particularly in large BB source regions (PSEA), would  
601 contribute to a deeper understanding of the uncertainties associated with fire emissions. In the PSEA region, greater attention  
602 should be given to the impacts of small fires, cloud cover, different ecosystem types, and EF during various burning stages  
603 and ecosystem types on the inversion of BB emission inventories. To further explore the subsequent effects of BB emissions  
604 (e.g., AOPs and radiative forcing), additional investigation of fire aerosol aging and treatment uncertainties (e.g., injection  
605 height, mixing state, SOA formation) are needed. Our study demonstrates that the uncertainty in BB emission inventories is  
606 an important factor influencing the WRF-Chem simulation of air quality and climate during wildfires, although the limitations  
607 of the model itself should not be overlooked. In the future, we will conduct additional sensitivity experiments and utilize more  
608 observational data to further validate the aforementioned uncertainties.

609

#### 610 **Data availability**

611 Global Fire Emissions Database, Version 4.1 (GFEDv4.1) are available at <https://doi.org/10.3334/ORNLDAAC/1293>  
612 (Randerson et al., 2017); The Fire INventory from NCAR (FINN, including version 1.5 and 2.5) data files can be downloaded  
613 from <https://www.acom.ucar.edu/Data/fire/> (Wiedinmyer et al., 2011); CAMS global biomass burning emissions based on fire  
614 radiative power (GFAS v1.2) at <https://ads.atmosphere.copernicus.eu/cdsapp#!/dataset/cams-global-fire-emissions-gfas>  
615 (Rémy et al., 2017); Fire Energetics and Emissions Research version 1.0 (FEER) data files can be downloaded from  
616 <https://feer.gsfc.nasa.gov/data/emissions/> (Ichoku and Ellison, 2014); Quick Fire Emissions Dataset version 2.5 release 1  
617 (QFED) data can be accessed from <https://portal.nccs.nasa.gov/datashare/iesa/aerosol/emissions/QFED/v2.5r1/> (Koster et al.,  
618 2015), and Integrated Monitoring and Modelling System for Wildland FIRES Project version 2.0 (IS4FIRES) data files can be  
619 downloaded from <http://silam.fmi.fi/thredds/catalog/i4f20emis-arch/catalog.html> (Soares et al., 2015).

#### 620 **Author contributions**

621 Conceptualization, methodology, and writing—original draft, Y.B.J.; Y.B.J. and Y.M.L. designed the research framework and  
622 collected the materials; Y.B.J. calculated the emissions and drew the figures; Y.M.L. and Y.B.J. analyzed the results and wrote  
623 the paper with inputs from all authors; All authors contributed to the discussion and improvement of the paper; Supervision,  
624 Q.F.





## 625 **Financial support**

626 This work was supported by the Guangdong Major Project of Basic and Applied Basic Research (Grant No.  
627 2020B0301030004), the National Key Research and Development Program of China (Grant No. 2019YFC0214605), Science  
628 and Technology Program of Guangdong Province (Science and Technology Innovation Platform Category) (Grant No.  
629 2019B121201002), and the National Natural Science Foundation of China (Grant No. 42075181).

## 630 **Competing interests**

631 The authors declare that they have no conflict of interest.

## 632 **References**

- 633 Akagi, S. K., Yokelson, R. J., Wiedinmyer, C., Alvarado, M. J., Reid, J. S., Karl, T., Crounse, J. D., and Wennberg, P. O.:  
634 Emission factors for open and domestic biomass burning for use in atmospheric models, *Atmos. Chem. Phys.*, 11, 4039-4072,  
635 10.5194/acp-11-4039-2011, 2011.
- 636 Andela, N., Kaiser, J. W., Heil, A., van Leeuwen, T. T., van der Werf, G. R., Wooster, M. J., Remy, S., and Schultz, M. G.:  
637 Assessment the Global Fire Assimilation System (GFASv1), MACC, Monitoring Atmospheric Composition and Climate II,  
638 urn:nbn:nl:ui:31-d103f7d8-9295-449f-8afd-6ae36c492b66, 2013.
- 639 Andreae, M. O.: Emission of trace gases and aerosols from biomass burning – an updated assessment, *Atmos. Chem. Phys.*,  
640 19, 8523-8546, 10.5194/acp-19-8523-2019, 2019.
- 641 Andreae, M. O. and Merlet, P.: Emission of trace gases and aerosols from biomass burning, 15, 955-966,  
642 <https://doi.org/10.1029/2000GB001382>, 2001.
- 643 Ångström, A.: On the Atmospheric Transmission of Sun Radiation and on Dust in the Air, *Geografiska Annaler*, 11, 156-166,  
644 10.1080/20014422.1929.11880498, 1929.
- 645 Archer-Nicholls, S., Lowe, D., Darbyshire, E., Morgan, W. T., Bela, M. M., Pereira, G., Trembath, J., Kaiser, J. W., Longo,  
646 K. M., Freitas, S. R., Coe, H., and McFiggans, G.: Characterising Brazilian biomass burning emissions using WRF-Chem with  
647 MOSAIC sectional aerosol, *Geosci. Model Dev.*, 8, 549-577, 10.5194/gmd-8-549-2015, 2015.
- 648 Baro, R., Palacios-Pena, L., Baklanov, A., Balzarini, A., Brunner, D., Forkel, R., Hirtl, M., Honzak, L., Perez, J. L., Pirovano,  
649 G., San Jose, R., Schroeder, W., Werhahn, J., Wolke, R., Zabkar, R., and Jimenez-Guerrero, P.: Regional effects of atmospheric  
650 aerosols on temperature: an evaluation of an ensemble of online coupled models, *Atmospheric Chemistry and Physics*, 17,  
651 9677-9696, 10.5194/acp-17-9677-2017, 2017.
- 652 Baró, R., Maurer, C., Brioude, J., Arnold, D., and Hirtl, M.: The Environmental Effects of the April 2020 Wildfires and the  
653 Cs-137 Re-Suspension in the Chernobyl Exclusion Zone: A Multi-Hazard Threat, 12, 467, 2021.
- 654 Buchholz, R., Emmons, L., Tilmes, S., and Team, T.: CESM2. 1/CAM-chem Instantaneous Output for Boundary Conditions.  
655 UCAR/NCAR—Atmospheric Chemistry Observations and Modeling Laboratory, <https://doi.org/10.5065/NMP7-EP60>, 2019.
- 656 Carter, T. S., Heald, C. L., Jimenez, J. L., Campuzano-Jost, P., Kondo, Y., Moteki, N., Schwarz, J. P., Wiedinmyer, C.,  
657 Darmenov, A. S., da Silva, A. M., and Kaiser, J. W.: How emissions uncertainty influences the distribution and radiative  
658 impacts of smoke from fires in North America, *Atmos. Chem. Phys.*, 20, 2073-2097, 10.5194/acp-20-2073-2020, 2020.
- 659 Chapman, E. G., Gustafson, W. I., Easter, R. C., Barnard, J. C., Ghan, S. J., Pekour, M. S., and Fast, J. D.: Coupling aerosol-  
660 cloud-radiative processes in the WRF-Chem model: Investigating the radiative impact of elevated point sources, *Atmospheric  
661 Chemistry and Physics*, 9, 945-964, 10.5194/acp-9-945-2009, 2009.
- 662 Chen, L., Zhu, J., Liao, H., Gao, Y., Qiu, Y., Zhang, M., Liu, Z., Li, N., and Wang, Y.: Assessing the formation and evolution  
663 mechanisms of severe haze pollution in the Beijing–Tianjin–Hebei region using process analysis, *Atmos. Chem. Phys.*, 19,  
664 10845-10864, 10.5194/acp-19-10845-2019, 2019.



- 665 Crippa, P., Sullivan, R., Thota, A., and Pryor, S. J. J. o. G. R. A.: Sensitivity of Simulated Aerosol Properties Over Eastern  
666 North America to WRF-Chem Parameterizations, 124, 3365-3383, 2019.
- 667 Dong, X. and Fu, J. S.: Understanding interannual variations of biomass burning from Peninsular Southeast Asia, part I: Model  
668 evaluation and analysis of systematic bias, Atmospheric Environment, 116, 293-307,  
669 <https://doi.org/10.1016/j.atmosenv.2015.06.026>, 2015a.
- 670 Dong, X. and Fu, J. S.: Understanding interannual variations of biomass burning from Peninsular Southeast Asia, part II:  
671 Variability and different influences in lower and higher atmosphere levels, Atmospheric Environment, 115, 9-18,  
672 <https://doi.org/10.1016/j.atmosenv.2015.05.052>, 2015b.
- 673 Dubovik, O. and King, M. D. J. J. o. G. R. A.: A flexible inversion algorithm for retrieval of aerosol optical properties from  
674 Sun and sky radiance measurements, 105, 20673-20696, 2000.
- 675 Emmons, L. K., Walters, S., Hess, P. G., Lamarque, J. F., Pfister, G. G., Fillmore, D., Granier, C., Guenther, A., Kinnison, D.,  
676 Laepple, T., Orlando, J., Tie, X., Tyndall, G., Wiedinmyer, C., Baughcum, S. L., and Kloster, S.: Description and evaluation  
677 of the Model for Ozone and Related chemical Tracers, version 4 (MOZART-4), Geosci. Model Dev., 3, 43-67, 10.5194/gmd-  
678 3-43-2010, 2010.
- 679 Emmons, L. K., Schwantes, R. H., Orlando, J. J., Tyndall, G., Kinnison, D., Lamarque, J.-F., Marsh, D., Mills, M. J., Tilmes,  
680 S., Bardeen, C., Buchholz, R. R., Conley, A., Gettelman, A., Garcia, R., Simpson, I., Blake, D. R., Meinardi, S., and Pétron,  
681 G.: The Chemistry Mechanism in the Community Earth System Model Version 2 (CESM2), 12, e2019MS001882,  
682 <https://doi.org/10.1029/2019MS001882>, 2020.
- 683 Fast, J. D., Gustafson Jr., W. I., Easter, R. C., Zaveri, R. A., Barnard, J. C., Chapman, E. G., Grell, G. A., and Peckham, S. E.:  
684 Evolution of ozone, particulates, and aerosol direct radiative forcing in the vicinity of Houston using a fully coupled  
685 meteorology-chemistry-aerosol model, 111, 10.1029/2005jd006721, 2006.
- 686 Filonchik, M., Peterson, M. P., and Sun, D.: Deterioration of air quality associated with the 2020 US wildfires, Science of The  
687 Total Environment, 826, 154103, <https://doi.org/10.1016/j.scitotenv.2022.154103>, 2022.
- 688 Freitas, S. R., Longo, K. M., Trentmann, J., and Latham, D.: Technical Note: Sensitivity of 1-D smoke plume rise models to  
689 the inclusion of environmental wind drag, Atmos. Chem. Phys., 10, 585-594, 10.5194/acp-10-585-2010, 2010.
- 690 Freitas, S. R., Longo, K. M., Chatfield, R., Latham, D., Silva Dias, M. A. F., Andreae, M. O., Prins, E., Santos, J. C., Gielow,  
691 R., and Carvalho Jr, J. A.: Including the sub-grid scale plume rise of vegetation fires in low resolution atmospheric transport  
692 models, Atmos. Chem. Phys., 7, 3385-3398, 10.5194/acp-7-3385-2007, 2007.
- 693 Ge, C., Wang, J., and Reid, J. S.: Mesoscale modeling of smoke transport over the Southeast Asian Maritime Continent:  
694 coupling of smoke direct radiative effect below and above the low-level clouds, Atmospheric Chemistry and Physics, 14, 159-  
695 174, 10.5194/acp-14-159-2014, 2014.
- 696 Grell, G., Freitas, S. R., Stuefer, M., and Fast, J.: Inclusion of biomass burning in WRF-Chem: impact of wildfires on weather  
697 forecasts, Atmospheric Chemistry and Physics, 11, 5289-5303, 10.5194/acp-11-5289-2011, 2011.
- 698 Grell, G. A. and Dévényi, D. J. G. R. L.: A generalized approach to parameterizing convection combining ensemble and data  
699 assimilation techniques, 29, 38-31-38-34, 2002.
- 700 Grell, G. A., Peckham, S. E., Schmitz, R., McKeen, S. A., Frost, G., Skamarock, W. C., and Eder, B.: Fully coupled "online"  
701 chemistry within the WRF model, Atmospheric Environment, 39, 6957-6975, 10.1016/j.atmosenv.2005.04.027, 2005.
- 702 Guenther, A. B., Jiang, X., Heald, C. L., Sakulyanontvittaya, T., Duhl, T., Emmons, L. K., and Wang, X.: The Model of  
703 Emissions of Gases and Aerosols from Nature version 2.1 (MEGAN2.1): an extended and updated framework for modeling  
704 biogenic emissions, Geosci. Model Dev., 5, 1471-1492, 10.5194/gmd-5-1471-2012, 2012.
- 705 Heil A., B. I.: ESA CCI ECV Fire Disturbance: D5.1 Product Validation and Intercomparison Report, version 2.1, 2020.
- 706 Hersbach, H., Bell, B., Berrisford, P., Biavati, G., Horányi, A., Muñoz Sabater, J., Nicolas, J., Peubey, C., Radu, R., and  
707 Rozum, I. J. C. c. c. s. c. d. s.: ERA5 hourly data on single levels from 1979 to present, 10, 2018.
- 708 Hu, Z. Y., Zhao, C., Huang, J. P., Leung, L. R., Qian, Y., Yu, H. B., Huang, L., and Kalashnikova, O. V.: Trans-Pacific  
709 transport and evolution of aerosols: evaluation of quasi-global WRF-Chem simulation with multiple observations,  
710 Geoscientific Model Development, 9, 1725-1746, 10.5194/gmd-9-1725-2016, 2016.
- 711 Huneus, N., Chevallier, F., and Boucher, O.: Estimating aerosol emissions by assimilating observed aerosol optical depth in  
712 a global aerosol model, Atmos. Chem. Phys., 12, 4585-4606, 10.5194/acp-12-4585-2012, 2012.



- 713 Iacono, M. J., Delamere, J. S., Mlawer, E. J., Shephard, M. W., Clough, S. A., and Collins, W. D.: Radiative forcing by long-  
714 lived greenhouse gases: Calculations with the AER radiative transfer models, 113, <https://doi.org/10.1029/2008JD009944>,  
715 2008.
- 716 Ichoku, C. and Ellison, L.: Global top-down smoke-aerosol emissions estimation using satellite fire radiative power  
717 measurements, *Atmos. Chem. Phys.*, 14, 6643-6667, 10.5194/acp-14-6643-2014, 2014.
- 718 Ichoku, C. and Kaufman, Y. J.: A method to derive smoke emission rates from MODIS fire radiative energy measurements,  
719 *IEEE Transactions on Geoscience and Remote Sensing*, 43, 2636-2649, 10.1109/TGRS.2005.857328, 2005.
- 720 Janjić, Z. I.: The Step-Mountain Coordinate: Physical Package %J *Monthly Weather Review*, 118, 1429-1443,  
721 [https://doi.org/10.1175/1520-0493\(1990\)118<1429:TSMCPP>2.0.CO;2](https://doi.org/10.1175/1520-0493(1990)118<1429:TSMCPP>2.0.CO;2), 1990.
- 722 Jathar, S. H., Gordon, T. D., Hennigan, C. J., Pye, H. O. T., Pouliot, G., Adams, P. J., Donahue, N. M., and Robinson, A. L.:  
723 Unspeciated organic emissions from combustion sources and their influence on the secondary organic aerosol budget in the  
724 United States, 111, 10473-10478, doi:10.1073/pnas.1323740111, 2014.
- 725 Southeastern Asia Ignited by Agricultural Fires, last
- 726 Jin, Y., Ma, Y., Zhang, M., Liu, Y., Lu, X., Liu, B., Jin, S., Shen, A., Zhang, J., and Fan, Q.: Aerosol Characteristics during  
727 the COVID-19 Lockdown in China: Optical Properties, Vertical Distribution, and Potential Source, 14, 3336, 2022.
- 728 Jose, R. S., Pérez, J. L., González, R. M., Pecci, J., and Palacios, M.: Improving air quality modelling systems by using on-  
729 line wild land fire forecasting tools coupled into WRF/Chem simulations over Europe, *Urban Climate*, 22, 2-18,  
730 <https://doi.org/10.1016/j.uclim.2016.09.001>, 2017.
- 731 Kang, L., Chen, S., Huang, J., Zhao, S., Ma, X., Yuan, T., Zhang, X., and Xie, T.: The Spatial and Temporal Distributions of  
732 Absorbing Aerosols over East Asia, *Remote Sens.*, 9, 1050, 2017.
- 733 Koster, R. D., Darmenov, A. S., and da Silva, A. M.: The quick fire emissions dataset (QFED): Documentation of versions  
734 2.1, 2.2 and 2.4, 2015.
- 735 Kumar, R., Barth, M. C., Pfister, G. G., Naja, M., and Brasseur, G. P.: WRF-Chem simulations of a typical pre-monsoon dust  
736 storm in northern India: influences on aerosol optical properties and radiation budget, *Atmospheric Chemistry and Physics*,  
737 14, 2431-2446, 10.5194/acp-14-2431-2014, 2014.
- 738 Lin, C.-Y., Zhao, C., Liu, X., Lin, N.-H., and Chen, W.-N.: Modelling of long-range transport of Southeast Asia biomass-  
739 burning aerosols to Taiwan and their radiative forcings over East Asia, *Tellus B: Chemical and Physical Meteorology*, 66,  
740 23733, 10.3402/tellusb.v66.23733, 2014.
- 741 Liu, T., Mickley, L. J., Marlier, M. E., DeFries, R. S., Khan, M. F., Latif, M. T., and Karambelas, A.: Diagnosing spatial biases  
742 and uncertainties in global fire emissions inventories: Indonesia as regional case study, *Remote Sensing of Environment*, 237,  
743 111557, <https://doi.org/10.1016/j.rse.2019.111557>, 2020.
- 744 Ma, Y., Jin, Y., Zhang, M., Gong, W., Hong, J., Jin, S., Shi, Y., Zhang, Y., and Liu, B.: Aerosol optical properties of haze  
745 episodes in eastern China based on remote-sensing observations and WRF-Chem simulations, *Science of The Total  
746 Environment*, 757, 143784, 10.1016/j.scitotenv.2020.143784, 2021.
- 747 Mallia, D. V., Kochanski, A. K., Urbanski, S. P., and Lin, J. C.: Optimizing Smoke and Plume Rise Modeling Approaches at  
748 Local Scales, 9, 166, 2018.
- 749 Marlier, M. E., DeFries, R. S., Voulgarakis, A., Kinney, P. L., Randerson, J. T., Shindell, D. T., Chen, Y., and Faluvegi, G.:  
750 El Niño and health risks from landscape fire emissions in southeast Asia, *Nature climate change*, 3, 131-136, 2013.
- 751 Martinez-Lozano, J., Utrillas, M., Tena, F., and Cachorro, V. J. S. E.: The parameterisation of the atmospheric aerosol optical  
752 depth using the Ångström power law, 63, 303-311, 1998.
- 753 EDGAR v5.0 emissions inventory speciated for the MOZART chemical mechanism, last
- 754 Mellor, G. L. and Yamada, T.: Development of a turbulence closure model for geophysical fluid problems, 20, 851-875,  
755 <https://doi.org/10.1029/RG020i004p00851>, 1982.
- 756 Monin, A. S. and Obukhov, A. M. J. C. G. I. A. S. U.: Basic laws of turbulent mixing in the surface layer of the atmosphere,  
757 151, e187, 1954.
- 758 Morrison, H., Curry, J. A., and Khvorostyanov, V. I.: A New Double-Moment Microphysics Parameterization for Application  
759 in Cloud and Climate Models. Part I: Description %J *Journal of the Atmospheric Sciences*, 62, 1665-1677,  
760 <https://doi.org/10.1175/JAS3446.1>, 2005.



- 761 Niu, G.-Y., Yang, Z.-L., Mitchell, K. E., Chen, F., Ek, M. B., Barlage, M., Kumar, A., Manning, K., Niyogi, D., Rosero, E.,  
762 Tewari, M., and Xia, Y.: The community Noah land surface model with multiparameterization options (Noah-MP): 1. Model  
763 description and evaluation with local-scale measurements, 116, <https://doi.org/10.1029/2010JD015139>, 2011.
- 764 Palacios-Pena, L., Baro, R., Luis Guerrero-Rascado, J., Alados-Arboledas, L., Brunner, D., and Jimenez-Guerrero, P.:  
765 Evaluating the representation of aerosol optical properties using an online coupled model over the Iberian Peninsula,  
766 *Atmospheric Chemistry and Physics*, 17, 277-296, [10.5194/acp-17-277-2017](https://doi.org/10.5194/acp-17-277-2017), 2017.
- 767 Palacios-Peña, L., Baró, R., Baklanov, A., Balzarini, A., Brunner, D., Forkel, R., Hirtl, M., Honzak, L., López-Romero, J. M.,  
768 Montávez, J. P. J. A. C., and Physics: An assessment of aerosol optical properties from remote-sensing observations and  
769 regional chemistry–climate coupled models over Europe, 18, 5021-5043, 2018.
- 770 Palacios-Peña, L., Jiménez-Guerrero, P., Baró, R., Balzarini, A., Bianconi, R., Curci, G., Landi, T. C., Pirovano, G., Prank,  
771 M., Riccio, A., Tuccella, P., and Galmarini, S.: Aerosol optical properties over Europe: an evaluation of the AQMEII Phase 3  
772 simulations against satellite observations, *Atmos. Chem. Phys.*, 19, 2965-2990, [10.5194/acp-19-2965-2019](https://doi.org/10.5194/acp-19-2965-2019), 2019.
- 773 Pan, X., Ichoku, C., Chin, M., Bian, H., Darmenov, A., Colarco, P., Ellison, L., Kucsera, T., da Silva, A., Wang, J., Oda, T.,  
774 and Cui, G.: Six global biomass burning emission datasets: intercomparison and application in one global aerosol model,  
775 *Atmos. Chem. Phys.*, 20, 969-994, [10.5194/acp-20-969-2020](https://doi.org/10.5194/acp-20-969-2020), 2020.
- 776 Randerson, J. T., Van Der Werf, G. R., Giglio, L., Collatz, G. J., and Kasibhatla, P. S.: Global Fire Emissions Database,  
777 Version 4.1 (GFEDv4), [10.3334/ORNLDAAC/1293](https://doi.org/10.3334/ORNLDAAC/1293), 2017.
- 778 Reddington, C. L., Conibear, L., Robinson, S., Knote, C., Arnold, S. R., and Spracklen, D. V.: Air Pollution From Forest and  
779 Vegetation Fires in Southeast Asia Disproportionately Impacts the Poor, 5, [e2021GH000418](https://doi.org/10.1029/2021GH000418),  
780 <https://doi.org/10.1029/2021GH000418>, 2021.
- 781 Reddington, C. L., Spracklen, D. V., Artaxo, P., Ridley, D. A., Rizzo, L. V., and Arana, A.: Analysis of particulate emissions  
782 from tropical biomass burning using a global aerosol model and long-term surface observations, *Atmos. Chem. Phys.*, 16,  
783 11083-11106, [10.5194/acp-16-11083-2016](https://doi.org/10.5194/acp-16-11083-2016), 2016.
- 784 Reddington, C. L., Morgan, W. T., Darbyshire, E., Brito, J., Coe, H., Artaxo, P., Scott, C. E., Marsham, J., and Spracklen, D.  
785 V.: Biomass burning aerosol over the Amazon: analysis of aircraft, surface and satellite observations using a global aerosol  
786 model, *Atmos. Chem. Phys.*, 19, 9125-9152, [10.5194/acp-19-9125-2019](https://doi.org/10.5194/acp-19-9125-2019), 2019.
- 787 Reid, J. S., Hyer, E. J., Johnson, R. S., Holben, B. N., Yokelson, R. J., Zhang, J., Campbell, J. R., Christopher, S. A., Di  
788 Girolamo, L., Giglio, L., Holz, R. E., Kearney, C., Miettinen, J., Reid, E. A., Turk, F. J., Wang, J., Xian, P., Zhao, G.,  
789 Balasubramanian, R., Chew, B. N., Janjai, S., Lagrosas, N., Lestari, P., Lin, N.-H., Mahmud, M., Nguyen, A. X., Norris, B.,  
790 Oanh, N. T. K., Oo, M., Salinas, S. V., Welton, E. J., and Liew, S. C.: Observing and understanding the Southeast Asian  
791 aerosol system by remote sensing: An initial review and analysis for the Seven Southeast Asian Studies (7SEAS) program,  
792 *Atmospheric Research*, 122, 403-468, <https://doi.org/10.1016/j.atmosres.2012.06.005>, 2013.
- 793 Rémy, S., Veira, A., Paugam, R., Sofiev, M., Kaiser, J. W., Marenco, F., Burton, S. P., Benedetti, A., Engelen, R. J., Ferrare,  
794 R., and Hair, J. W.: Two global data sets of daily fire emission injection heights since 2003, *Atmos. Chem. Phys.*, 17, 2921-  
795 2942, [10.5194/acp-17-2921-2017](https://doi.org/10.5194/acp-17-2921-2017), 2017.
- 796 Saide, P. E., Mena-Carrasco, M., Tolvett, S., Hernandez, P., and Carmichael, G. R.: Air quality forecasting for winter-time  
797 PM<sub>2.5</sub> episodes occurring in multiple cities in central and southern Chile, *Journal of Geophysical Research-Atmospheres*, 121,  
798 558-575, [10.1002/2015jd023949](https://doi.org/10.1002/2015jd023949), 2016.
- 799 Saide, P. E., Carmichael, G. R., Liu, Z., Schwartz, C. S., Lin, H. C., da Silva, A. M., and Hyer, E.: Aerosol optical depth  
800 assimilation for a size-resolved sectional model: impacts of observationally constrained, multi-wavelength and fine mode  
801 retrievals on regional scale analyses and forecasts, *Atmospheric Chemistry and Physics*, 13, 10425-10444, [10.5194/acp-13-  
802 10425-2013](https://doi.org/10.5194/acp-13-10425-2013), 2013.
- 803 Sayer, A. M., Hsu, N. C., Lee, J., Kim, W. V., and Dutcher, S. T.: Validation, Stability, and Consistency of MODIS Collection  
804 6.1 and VIIRS Version 1 Deep Blue Aerosol Data Over Land, 124, 4658-4688, <https://doi.org/10.1029/2018JD029598>, 2019.
- 805 Smirnov, A., Holben, B. N., Eck, T. F., Dubovik, O., and Slutsker, I.: Cloud-Screening and Quality Control Algorithms for  
806 the AERONET Database, *Remote Sensing of Environment*, 73, 337-349, [https://doi.org/10.1016/S0034-4257\(00\)00109-7](https://doi.org/10.1016/S0034-4257(00)00109-7),  
807 2000.
- 808 Soares, J., Sofiev, M., and Hakkarainen, J.: Uncertainties of wild-land fires emission in AQMEII phase 2 case study,  
809 *Atmospheric Environment*, 115, 361-370, <https://doi.org/10.1016/j.atmosenv.2015.01.068>, 2015.





- 810 Sofiev, M., Vankevich, R., Lotjonen, M., Prank, M., Petukhov, V., Ermakova, T., Koskinen, J., and Kukkonen, J.: An  
811 operational system for the assimilation of the satellite information on wild-land fires for the needs of air quality modelling and  
812 forecasting, *Atmos. Chem. Phys.*, 9, 6833-6847, 10.5194/acp-9-6833-2009, 2009.
- 813 Su, X., Wei, Y., Wang, L., Zhang, M., Jiang, D., and Feng, L.: Accuracy, stability, and continuity of AVHRR, SeaWiFS,  
814 MODIS, and VIIRS deep blue long-term land aerosol retrieval in Asia, *Science of The Total Environment*, 832, 155048,  
815 <https://doi.org/10.1016/j.scitotenv.2022.155048>, 2022.
- 816 Torres, O., Jethva, H., Ahn, C., Jaross, G., and Loyola, D. G. J. A. M. T.: TROPOMI aerosol products: evaluation and  
817 observations of synoptic-scale carbonaceous aerosol plumes during 2018–2020, 13, 6789-6806, 2020.
- 818 Veeffkind, J. P., Aben, I., McMullan, K., Förster, H., de Vries, J., Otter, G., Claas, J., Eskes, H. J., de Haan, J. F., Kleipool, Q.,  
819 van Weele, M., Hasekamp, O., Hoogeveen, R., Landgraf, J., Snel, R., Tol, P., Ingmann, P., Voors, R., Kruizinga, B., Vink, R.,  
820 Visser, H., and Levelt, P. F.: TROPOMI on the ESA Sentinel-5 Precursor: A GMES mission for global observations of the  
821 atmospheric composition for climate, air quality and ozone layer applications, *Remote Sensing of Environment*, 120, 70-83,  
822 <https://doi.org/10.1016/j.rse.2011.09.027>, 2012.
- 823 Vongruang, P., Wongwises, P., and Pimonsree, S.: Assessment of fire emission inventories for simulating particulate matter  
824 in Upper Southeast Asia using WRF-CMAQ, *Atmospheric Pollution Research*, 8, 921-929,  
825 <https://doi.org/10.1016/j.apr.2017.03.004>, 2017.
- 826 Wang, J., Yue, Y., Wang, Y., Ichoku, C., Ellison, L., and Zeng, J.: Mitigating Satellite-Based Fire Sampling Limitations in  
827 Deriving Biomass Burning Emission Rates: Application to WRF-Chem Model Over the Northern sub-Saharan African Region,  
828 123, 507-528, <https://doi.org/10.1002/2017JD026840>, 2018.
- 829 Wiedinmyer, C., Akagi, S. K., Yokelson, R. J., Emmons, L. K., Al-Saadi, J. A., Orlando, J. J., and Soja, A. J.: The Fire  
830 INventory from NCAR (FINN): a high resolution global model to estimate the emissions from open burning, *Geosci. Model  
831 Dev.*, 4, 625-641, 10.5194/gmd-4-625-2011, 2011.
- 832 Wiedinmyer, C., Kimura, Y., McDonald-Buller, E. C., Emmons, L. K., Buchholz, R. R., Tang, W., Seto, K., Joseph, M. B.,  
833 Barsanti, K. C., Carlton, A. G., and Yokelson, R.: The Fire Inventory from NCAR version 2.5: an updated global fire emissions  
834 model for climate and chemistry applications, *EGUsphere*, 2023, 1-45, 10.5194/egusphere-2023-124, 2023.
- 835 Wu, J., Bei, N., Hu, B., Liu, S., Zhou, M., Wang, Q., Li, X., Lang, L., Tian, F., Liu, Z. J. A. C., and Physics: Aerosol–radiation  
836 feedback deteriorates the wintertime haze in the North China Plain, 19, 8703-8719, 2019.
- 837 Yadav, I. C., Linthoingambi Devi, N., Li, J., Syed, J. H., Zhang, G., and Watanabe, H.: Biomass burning in Indo-China  
838 peninsula and its impacts on regional air quality and global climate change-a review, *Environmental Pollution*, 227, 414-427,  
839 <https://doi.org/10.1016/j.envpol.2017.04.085>, 2017.
- 840 Yang, C. J. B.: Relocating labour-intensive manufacturing firms from China to Southeast Asia: A preliminary investigation,  
841 3, 1-13, 2016.
- 842 Yevich, R. and Logan, J. A.: An assessment of biofuel use and burning of agricultural waste in the developing world, 17,  
843 <https://doi.org/10.1029/2002GB001952>, 2003.
- 844 Yin, S.: Biomass burning spatiotemporal variations over South and Southeast Asia, *Environment International*, 145, 106153,  
845 <https://doi.org/10.1016/j.envint.2020.106153>, 2020.
- 846 Zhang, F., Wang, J., Ichoku, C., Hyer, E. J., Yang, Z., Ge, C., Su, S., Zhang, X., Kondragunta, S., Kaiser, J. W., Wiedinmyer,  
847 C., and da Silva, A.: Sensitivity of mesoscale modeling of smoke direct radiative effect to the emission inventory: a case study  
848 in northern sub-Saharan African region, *Environmental Research Letters*, 9, 075002, 10.1088/1748-9326/9/7/075002, 2014.
- 849 Zhang, L., Zhao, T., Gong, S., Kong, S., Tang, L., Liu, D., Wang, Y., Jin, L., Shan, Y., Tan, C., Zhang, Y., and Guo, X.:  
850 Updated emission inventories of power plants in simulating air quality during haze periods over East China, *Atmos. Chem.  
851 Phys.*, 18, 2065-2079, 10.5194/acp-18-2065-2018, 2018.
- 852 Zhao, C., Liu, X., Ruby Leung, L., and Hagos, S.: Radiative impact of mineral dust on monsoon precipitation variability over  
853 West Africa, *Atmos. Chem. Phys.*, 11, 1879-1893, 10.5194/acp-11-1879-2011, 2011.
- 854 Zhao, C., Leung, L. R., Easter, R., Hand, J., and Avise, J.: Characterization of speciated aerosol direct radiative forcing over  
855 California, *Journal of Geophysical Research-Atmospheres*, 118, 2372-2388, 10.1029/2012jd018364, 2013.
- 856 Zhao, C., Liu, X., Leung, L. R., Johnson, B., McFarlane, S. A., Gustafson, W. I., Fast, J. D., and Easter, R.: The spatial  
857 distribution of mineral dust and its shortwave radiative forcing over North Africa: modeling sensitivities to dust emissions and  
858 aerosol size treatments, *Atmospheric Chemistry and Physics*, 10, 8821-8838, 10.5194/acp-10-8821-2010, 2010.



859 Zhu, J., Xia, X., Wang, J., Zhang, J., Wiedinmyer, C., Fisher, J. A., and Keller, C. A.: Impact of Southeast Asian smoke on  
860 aerosol properties in Southwest China: First comparison of model simulations with satellite and ground observations, 122,  
861 3904-3919, <https://doi.org/10.1002/2016JD025793>, 2017.  
862

863 **Appendix A**

864 Abbreviations and Acronyms

AAOD	Absorbing aerosol optical depth
AEC	Aerosol extinction coefficient
AHAOD	Adjacent HAOD area
AOD	Aerosol optical depth
AOPs	Aerosol optical properties
ATM	In the atmosphere
BB	Biomass burning
BC	Black carbon
CALIPSO	Cloud-Aerosol Lidar and Infrared Pathfinder Satellite Observation
CAM-chem	Community Atmosphere Model with Chemistry
DA	Downwind area
DRF	Direct radiative forcing
DM	Dry matter
EDGAR	Emissions Database for Global Atmospheric Research
EF	Emission factors
FEER	Fire Energetics and Emissions Research
FINN	Fire INventory from NCAR
FRP	Fire radiative power
GEOS-Chem	Goddard Earth Observing System-Chemistry
GFAS	Global Fire Assimilation System
GFED	Global Fire Emissions Database
HAOD	High AOD
IS4FIRES	Integrated Monitoring and Modelling System for Wildland FIRES Project
LW	Longwave
MEGAN	Model of Emissions of Gases and Aerosols from Nature
MODIS	Moderate Resolution Imaging Spectroradiometer
MOSAIC	Model for Simulating Aerosol Interactions and Chemistry





MOZART	The Model for Ozone and Related chemical Tracers
NMHCs	Non-methane hydrocarbons
NMVOCs	Non-methane volatile organic compounds
OC	Organic carbon
OVOCs	Oxygenated volatile organic compounds
PSEA	Peninsular Southeast Asia
PM	Particulate matter
QFED	Quick Fire Emissions Dataset
RH2	2 m relative humidity
SFC	At the surface
SOA	Secondary organic aerosol
SSA	Single scattering albedo
SW	Shortwave
T2	2 m temperature
TOA	The top of the atmosphere
TPM	Total particle matter
VIIRS	Visible Infrared Imaging Radiometer Suite
WS10	10 m wind speed

865  
866



867 Tables

868 **Table 1. Comprehensive comparison of eight BB emission inventories globally in terms of different methodological details and**  
 869 **species, where Bottom-up approach to construct emission inventories are GFED v4.1s, FINN v1.5, FINN v2.5 MOS, FINN v2.5**  
 870 **MOSVIS, and others are Top-down approach.**

BB dataset	Resolution Temporal	Data source	Main EF <sup>a</sup>	OVOCs <sup>b</sup>	NMHCs <sup>c</sup>	Gas	Aerosols
GFED v4.1s	0.25°x 0.25°	MODIS C5	Akagi et al. (2011),	CH <sub>3</sub> COCHO, CH <sub>3</sub> COOH,etc	C <sub>2</sub> H <sub>4</sub> ,C <sub>2</sub> H <sub>6</sub> , C <sub>3</sub> H <sub>8</sub> , etc	CO, NO <sub>x</sub> , SO <sub>2</sub> , NH <sub>3</sub>	OC, BC, PM <sub>2.5</sub>
	3-hourly		Andreae and				
	daily		Merlet (2001) with updates				
FINN v1.5	1 km <sup>2</sup>	MODIS C6	Akagi et al. (2011),	CH <sub>3</sub> COCHO, CH <sub>3</sub> COOH,etc	C <sub>2</sub> H <sub>4</sub> ,C <sub>2</sub> H <sub>6</sub> , C <sub>3</sub> H <sub>8</sub> , etc	CO, NO <sub>x</sub> , SO <sub>2</sub> , NH <sub>3</sub>	OC, BC, PM <sub>2.5</sub> ,PM <sub>10</sub>
	Daily		Andreae and Merlet (2001)				
FINN v2.5 MOS	1 km <sup>2</sup>	MODIS C6	Akagi et al. (2011),	CH <sub>3</sub> COCHO, CH <sub>3</sub> COOH,etc	C <sub>2</sub> H <sub>4</sub> ,C <sub>2</sub> H <sub>6</sub> , C <sub>3</sub> H <sub>8</sub> , etc	CO, NO <sub>x</sub> , SO <sub>2</sub> , NH <sub>3</sub>	OC, BC, PM <sub>2.5</sub> , PM <sub>10</sub>
	Daily		Wiedinmyer et al (2011)				
FINN v2.5 MOSVIS	1 km <sup>2</sup>	MODIS C6 VIIRS	Akagi et al. (2011),	CH <sub>3</sub> COCHO, CH <sub>3</sub> COOH,etc	C <sub>2</sub> H <sub>4</sub> ,C <sub>2</sub> H <sub>6</sub> , C <sub>3</sub> H <sub>8</sub> , etc	CO, NO <sub>x</sub> , SO <sub>2</sub> , NH <sub>3</sub>	OC, BC, PM <sub>2.5</sub> , PM <sub>10</sub>
	Daily		Wiedinmyer et al (2011)				
GFAS v1.2	0.1°x 0.1°	MODIS C6	Akagi et al. (2011)	CH <sub>3</sub> COCHO, CH <sub>3</sub> COOH,etc	C <sub>2</sub> H <sub>4</sub> ,C <sub>2</sub> H <sub>6</sub> , C <sub>3</sub> H <sub>8</sub> , etc	CO, NO <sub>x</sub> , SO <sub>2</sub> , NH <sub>3</sub>	OC, BC, PM <sub>2.5</sub>
	Daily						
FEER v1.0-G1.2	0.1°x 0.1°	GFAS v1.2 FRP	Andreae and Merlet (2001)	CH <sub>3</sub> COCHO, CH <sub>3</sub> COOH,etc	C <sub>2</sub> H <sub>2</sub> ,C <sub>2</sub> H <sub>6</sub> , C <sub>3</sub> H <sub>8</sub> , etc	CO, NO <sub>x</sub> , SO <sub>2</sub> , NH <sub>3</sub>	OC, BC, PM <sub>2.5</sub>
	Daily						
QFED v2.5r1	0.1°x 0.1°	MODIS C6	Akagi et al., (2011), Andreae and Merlet, (2001)	CH <sub>3</sub> COCHO, CH <sub>3</sub> COOH,etc	C <sub>2</sub> H <sub>6</sub> ,C <sub>3</sub> H <sub>6</sub> , C <sub>3</sub> H <sub>8</sub> , etc	CO, NO <sub>x</sub> , SO <sub>2</sub> , NH <sub>3</sub>	OC, BC, PM <sub>2.5</sub>
	Daily						
IS4FIRES v2.0	0.1°x 0.1°	MODIS C6	Akagi et al. (2011), Sofiev et al., (2009)	NA	NA	NA	TPM <sup>d</sup>
	3-hourly						
	2000-Present						

871 <sup>a</sup>The main references for Emission factors (EF) used in the BB emission database.

872 <sup>b</sup>Oxygenated volatile organic compounds (OVOCs) contain C, H, and O. examples include alcohols, aldehydes, ketones, and organic  
 873 acids.

874 <sup>c</sup>Non-methane hydrocarbons (NMHCs) are defined as organic compounds excluding methane (CH<sub>4</sub>) that contain only C and H.

875 <sup>d</sup>The total particle matter (TPM) considers three different particle sizes (0.17 μm, 1.1 μm and 3 μm).

876 **Notes: OVOCs and NMHCs together account for nearly all the gas-phase non-methane volatile organic compounds (NMVOC)**  
 877 **emitted by fires (Akagi et al., 2011). NA: Not available.**



878 **Table 2. WRF-Chem AOD and AAOD vs. satellites evaluation in HAOD (97-110°E, 15-22.5°N) region during March 2019.**

BB Inventories	WRF-Chem vs. VIIRS			WRF-Chem vs. TROPOMI		
	MB	RMSE	R	MB	RMSE	R
GFED	-0.26	0.48	0.22	0.009	0.018	0.191
FINN1.5	0.39	0.71	0.27	0.056	0.071	0.190
FINN2.5 MOS	0.63	0.98	0.27	0.073	0.094	0.205
FINN2.5 MOSVIS	0.78	1.01	0.28	0.080	0.102	0.232
GFAS	-0.34	0.52	0.21	0.004	0.013	0.185
FEER	-0.12	0.44	0.25	0.020	0.029	0.213
QFED	-0.24	0.46	0.23	0.011	0.020	0.187
IS4FIRES	-0.14	0.43	0.27	0.018	0.028	0.208

879  
 880  
 881  
 882  
 883  
 884  
 885  
 886  
 887  
 888  
 889  
 890  
 891  
 892  
 893  
 894  
 895  
 896  
 897  
 898  
 899  
 900



901  
902

**Table 3. WRF-Chem AOD at 550 nm vs. AERONET in HAOD, AHAOD, and DA during the wildfire period, where HAOD includes Laos, Chiang Mai, Doi Ang Khang, Fang, Nong Khai, Son La, and Ubon Ratchathani stations.**

Stations	Variables	BB emission inventories							
		GFED	FINN1.5	FINN2.5 MOS	FINN2.5 MOSVIS	GFAS	FEER	QFED	IS4FIRES
Laos	R	0.74	0.9	0.9	0.81	0.7	0.84	0.79	0.85
	IOA	0.78	0.83	0.75	0.75	0.76	0.84	0.8	0.86
Chiang Mai	R	0.46	0.61	0.53	0.77	0.48	0.54	0.45	0.55
	IOA	0.75	0.79	0.74	0.82	0.73	0.77	0.76	0.78
Doi Ang Khang	R	0.48	0.66	0.66	0.8	0.49	0.64	0.52	0.63
	IOA	0.78	0.75	0.68	0.69	0.77	0.81	0.79	0.81
Fang	R	0.42	0.71	0.7	0.85	0.42	0.68	0.5	0.63
	IOA	0.71	0.81	0.77	0.82	0.7	0.73	0.71	0.75
Nong Khai	R	0.25	0.39	0.59	0.51	0.28	0.27	0.31	0.37
	IOA	0.73	0.71	0.69	0.65	0.71	0.72	0.73	0.74
Son La	R	0.5	0.75	0.76	0.64	0.43	0.81	0.64	0.64
	IOA	0.72	0.72	0.65	0.65	0.71	0.84	0.75	0.79
Ubon Ratchath ani	R	0.23	0.6	0.54	0.3	0.41	0.35	0.36	0.37
	IOA	0.68	0.64	0.61	0.58	0.64	0.69	0.66	0.69
AHBA	$\bar{R}$	0.44	0.51	0.48	0.24	0.53	0.52	0.55	0.52
	$\overline{IOA}$	0.73	0.69	0.66	0.63	0.72	0.76	0.75	0.74
DA	$\bar{R}$	0.43	0.41	0.39	0.48	0.44	0.44	0.46	0.39
	$\overline{IOA}$	0.69	0.71	0.69	0.71	0.69	0.71	0.70	0.70

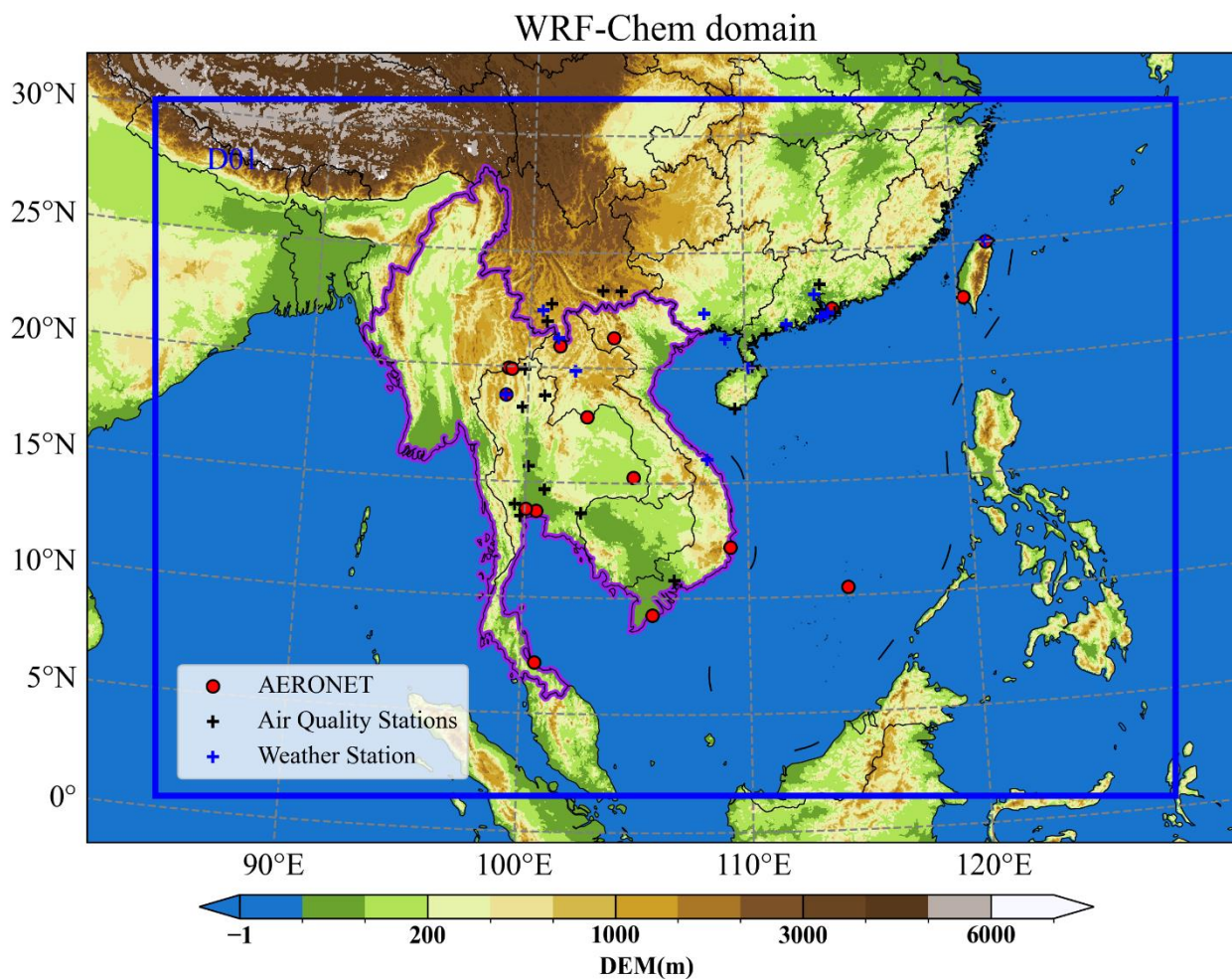
903 Note: AHAOD and DA only contain the corresponding site mean R and IOA

904



905  
906

## Figures



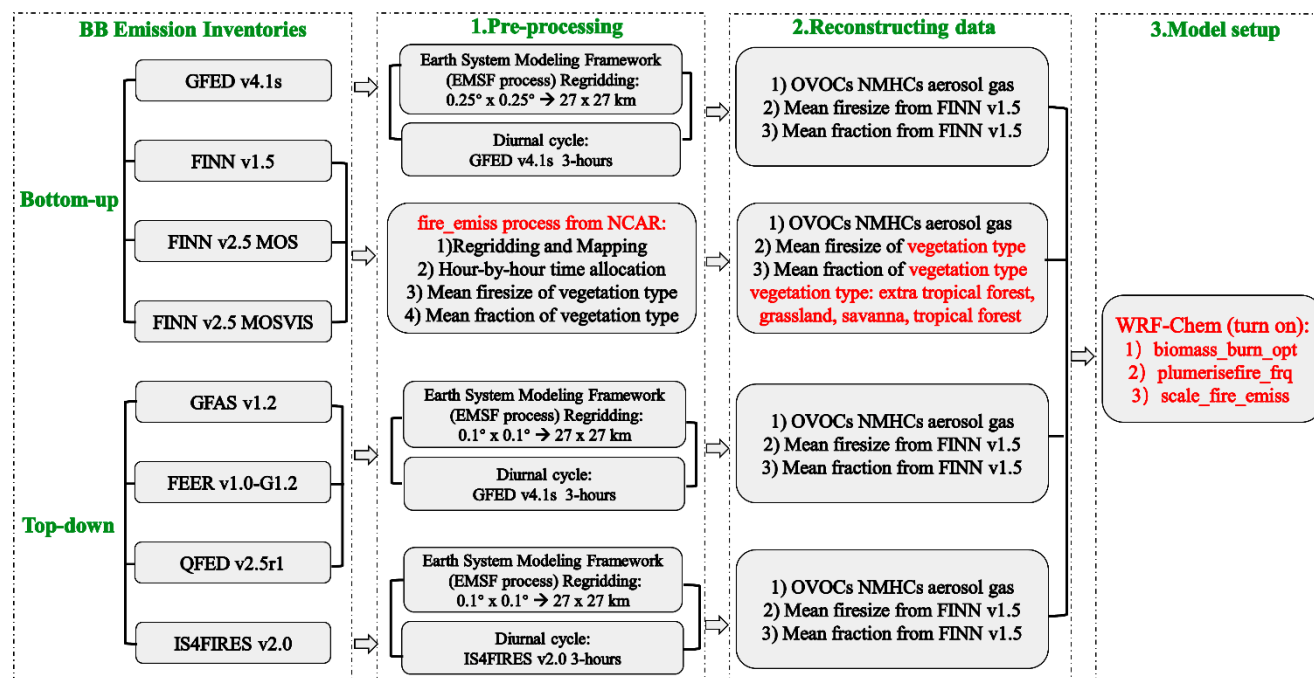
907

908 **Figure 1.** WRF-Chem simulation domain (D01, blue line), which is mainly the PSEA region (purple line, including Vietnam, Thailand,  
909 Myanmar, Cambodia, and Laos), South China Sea, and South China region, where the red dots are AERONET stations, the black  
910 crosses are air quality stations, and the blue crosses are meteorological stations.

911



912

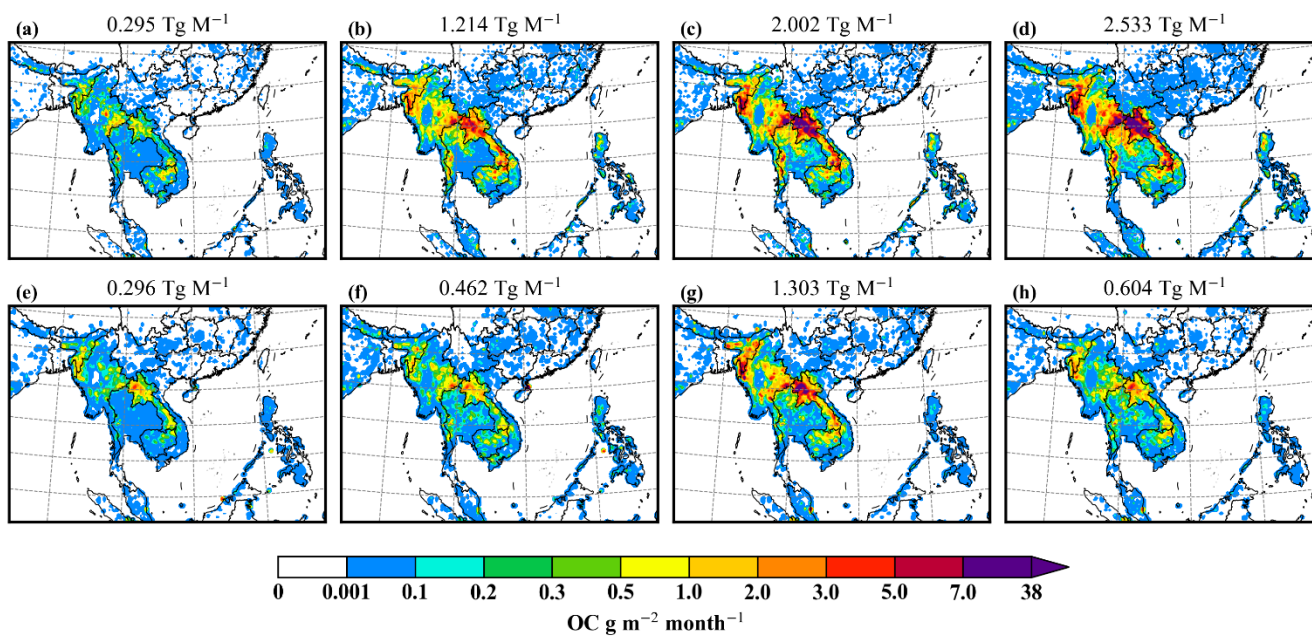


913  
 914  
 915  
 916  
 917  
 918  
 919  
 920  
 921  
 922  
 923  
 924

**Figure 2.** The flowchart illustrates the three processes of Pre-processing, Reconstructing data, and Model setup to put the eight BB emission inventories into the WRF-Chem simulation of AOPs and DRFs during the March 2019 wildfires in the PSEA region. The Pre-processing consisted of re-gridding and time allocation, where the FINNs scenario was processed using the fire\_emiss program from NCAR, while the grids generated by the other scenarios based on the FINN 1.5 scenario were spatially allocated using the EMSF program. The GFED, GFAS, FEER, and QFED have the same time allocations as GFED, and the remainder use self-contained time allocations. The Reconstructing data has three components: emissions (OVOCs, NMHCs, aerosol, and gas) composed by the MOZART-MOSAIC mechanism, fire size, and vegetation proportions (extratropical forest, grassland, savanna, tropical forest). Compared to the FINNs scheme, the missing compounds and aerosols from the other schemes were added based on the methodology of Jose et al. (2017), Andreae and Merlet (2001;2019). Eight BB emission inventories used the fire sizes provided by the FINN 1.5 scheme, as well as the vegetation proportions. The Model setup turned on BB simulations including the smoke plume rise.

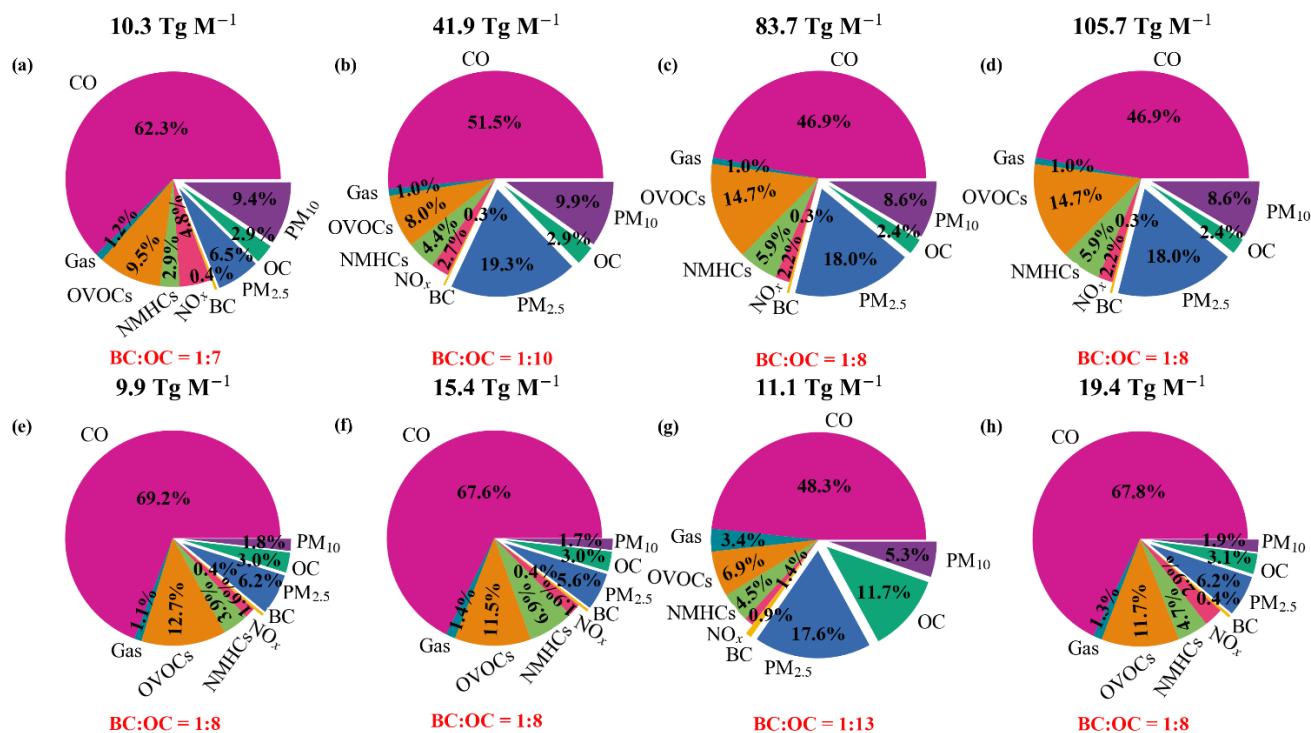
925





926

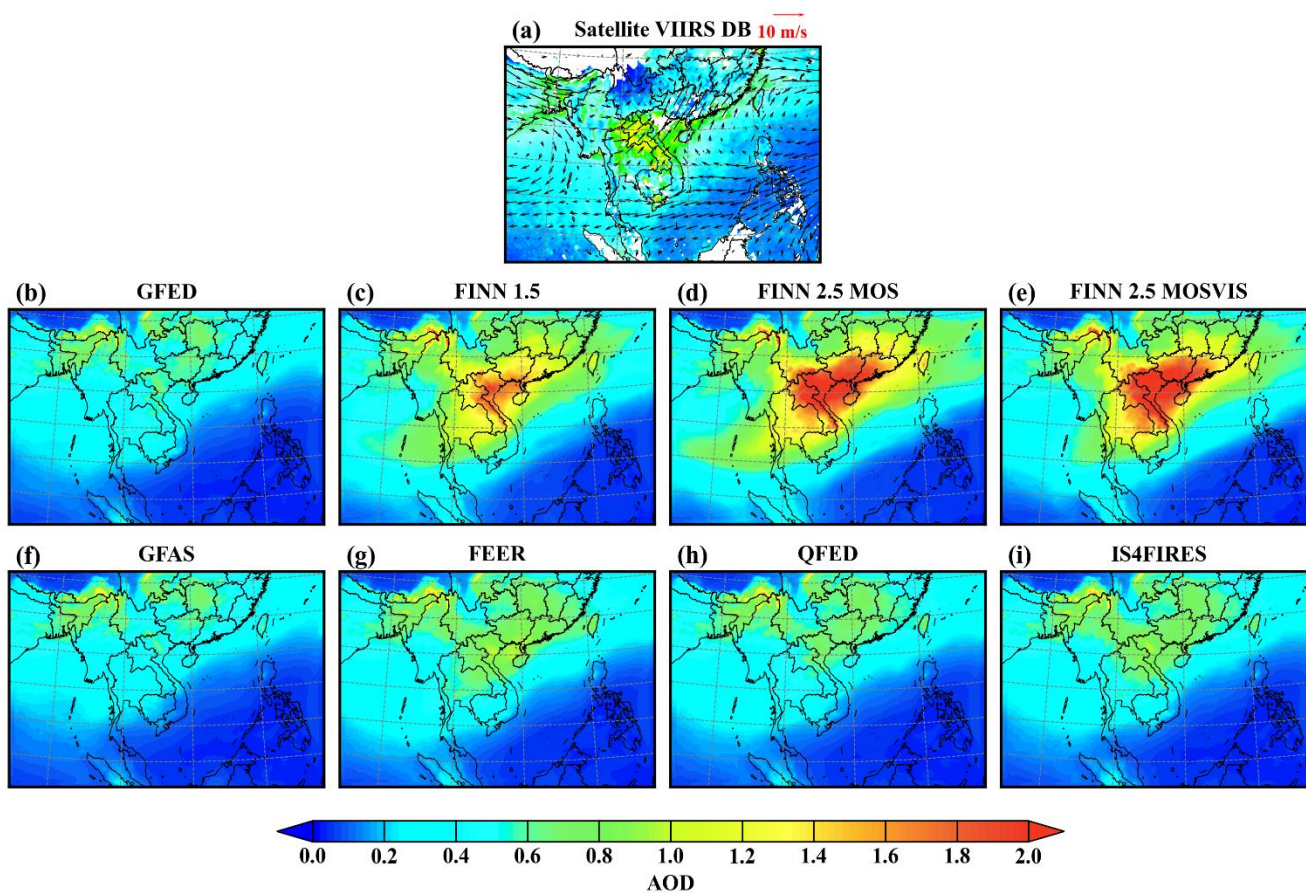
927 **Figure 3. The spatial distribution of eight BB emission inventories of OC in the study region, for (a-h): GFED, FINN1.5, FINN2.5**  
928 **MOS, FINN2.5 MOSVIS, GFAS, FEER, QFED, IS4FIRES, and the total OC emissions in the PSEA region during March 2019.**



929

930  
 931  
 932  
 933  
 934  
 935  
 936  
 937  
 938  
 939

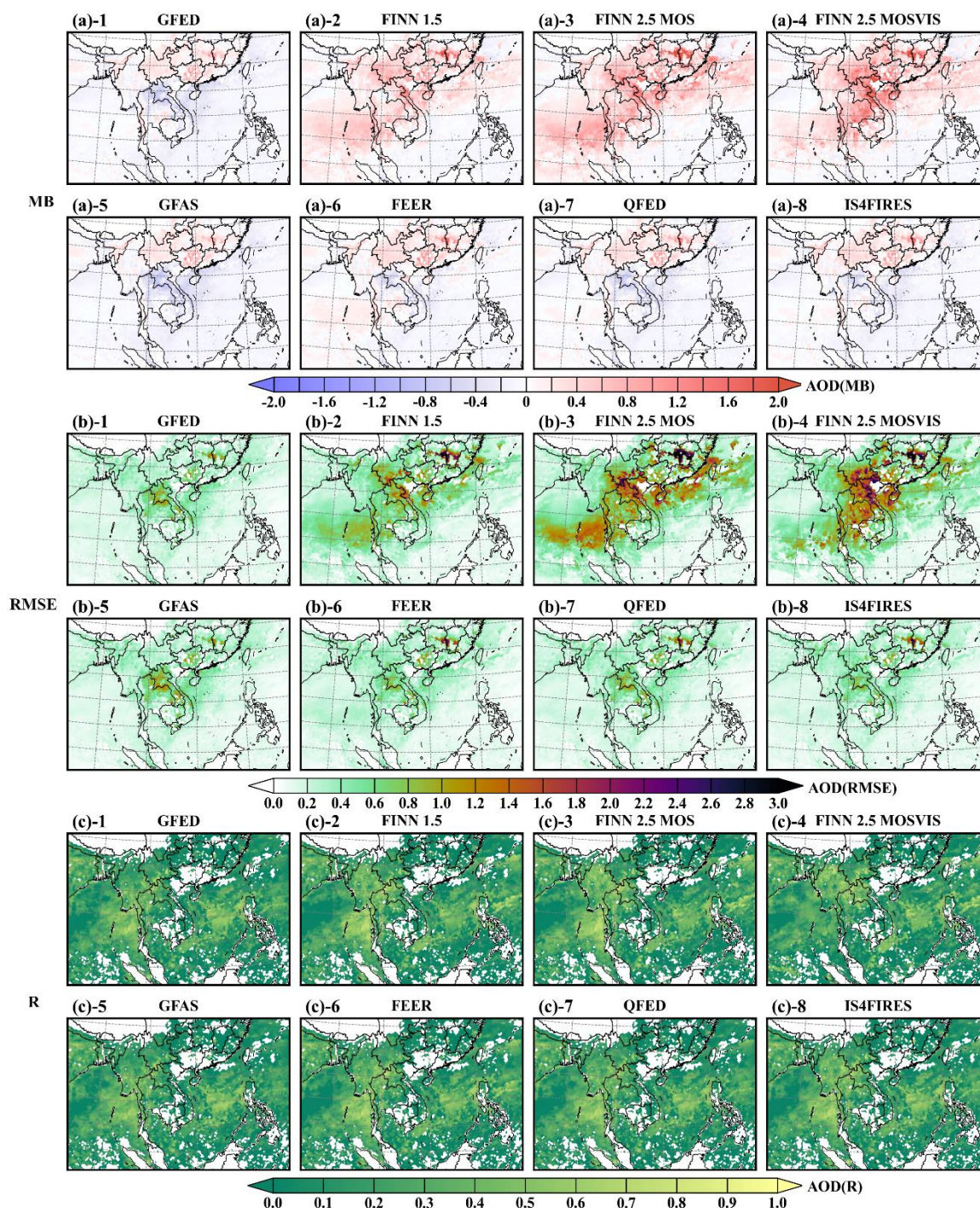
**Figure 4.** Total emissions and percentage composition of different substances in the eight BB emission inventories (after processing in Figure 2, i.e., the missing BB data has been supplemented.) over PSEA in the WRF-Chem model, which indicates the proportion of BC and OC, where "Gas" represents the combination of SO<sub>2</sub> and NH<sub>3</sub>. OVOCs contain C, H, and O compounds (ethanol (C<sub>2</sub>H<sub>5</sub>OH), formaldehyde (CH<sub>2</sub>O), acetaldehyde (CH<sub>3</sub>CHO), acetone (CH<sub>3</sub>COCH<sub>3</sub>), methanol (CH<sub>3</sub>OH), methyl ethyl ketone (MEK), pentanediol (C<sub>5</sub>H<sub>12</sub>O<sub>2</sub>), acetic acid (CH<sub>3</sub>COOH), cresol (C<sub>6</sub>H<sub>4</sub>(CH<sub>3</sub>)(OH)), glyceraldehyde (GLYALD), methanal (Mgly), glyoxal (CH<sub>2</sub>COCHO), acetol (CH<sub>3</sub>COCH<sub>2</sub>OH), methyl vinyl ketone (MACR), methyl vinyl ketone (MVK)). NMHCs refer to organic compounds containing only C and H besides methane (CH<sub>4</sub>), including pentane (C<sub>5</sub>H<sub>12</sub>), butadiene (C<sub>4</sub>H<sub>8</sub>), ethylene (C<sub>2</sub>H<sub>4</sub>), ethane (C<sub>2</sub>H<sub>6</sub>), propane (C<sub>3</sub>H<sub>8</sub>), propylene (C<sub>3</sub>H<sub>6</sub>), toluene (C<sub>6</sub>H<sub>5</sub>(CH<sub>3</sub>)), decane (C<sub>10</sub>H<sub>16</sub>), isoprene (C<sub>5</sub>H<sub>8</sub>). NMHCs and OVOCs combined constitute nearly all of the non-methane volatile organic compounds (NMVOCs) emitted by wildfires. PM<sub>2.5</sub> is the PM<sub>2.5</sub> fraction excluding OC and BC. PM<sub>10</sub> is the PM<sub>10-2.5</sub> fraction.



940  
941 **Figure 5.** The daily mean AOD retrieved by the VIIRS satellite (a) transiting the PSEA region and the AOD simulated by WRF-  
942 Chem with eight corresponding BB emission inventories (b-i, GFED, FINN1.5, FINN2.5 MOS, FINN2.5 MOSVIS, GFAS, FEER,  
943 QFED, IS4FIRES) in the PSEA region during March 2019, where 950 hPa wind (vectors, m/s) based on March 2019 of ERA5 data.

944  
945  
946  
947  
948  
949  
950  
951  
952  
953



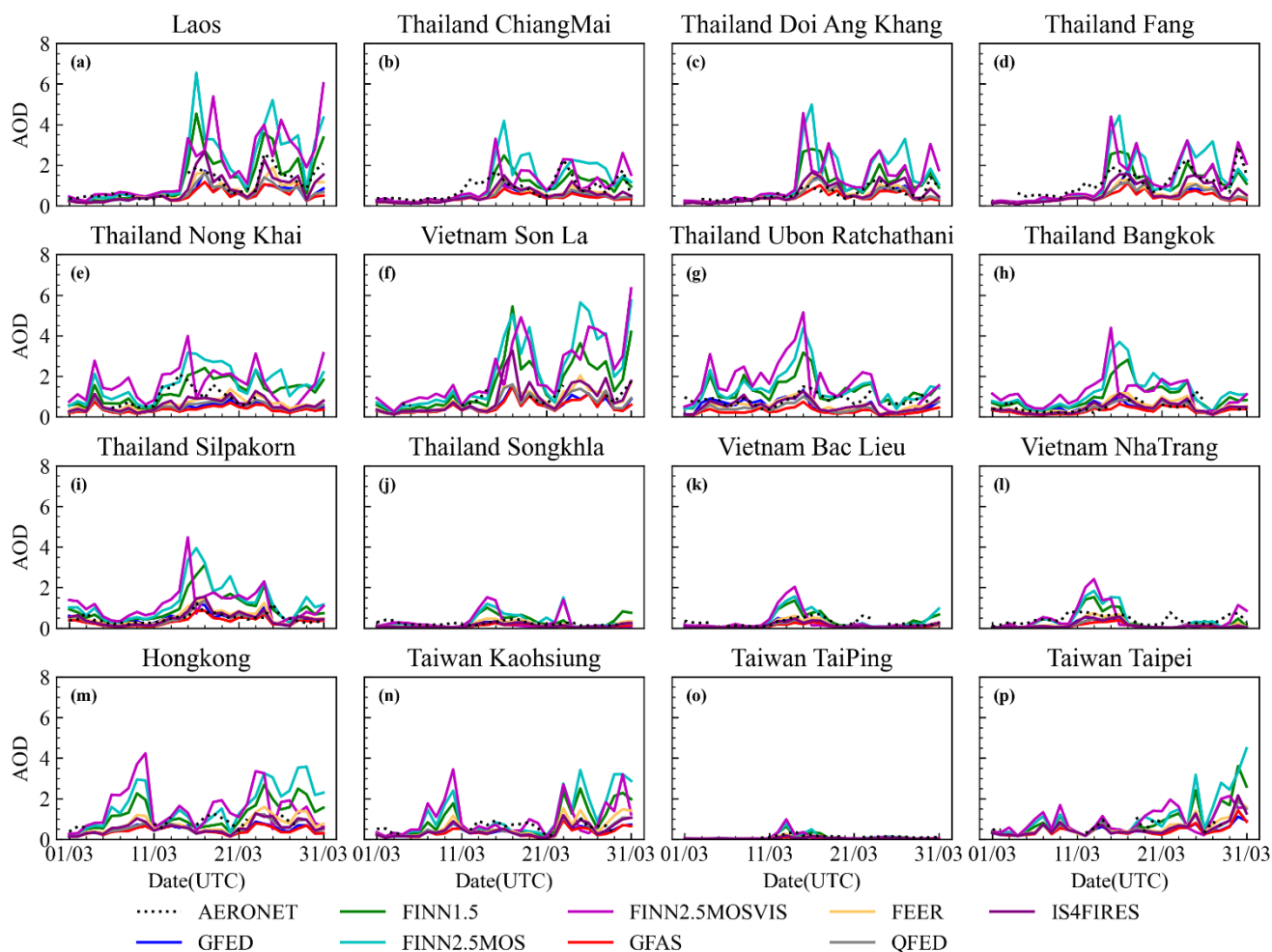


954

955 **Figure 6. Spatial distribution of MB, RMSE, and R between AOD from VIIRS satellite vs. AOD simulated by WRF-Chem with 8**  
 956 **BB emission inventories (GFED, FINN1.5, FINN2.5 MOS, FINN2.5 MOSVIS, GFAS, FEER, QFED, IS4FIRES) in PSEA during**  
 957 **March 2019, where (a)-1 to (a)-8 are the MB for the comparison of the eight BB scenarios, (b)-1 to (b)-8 are the RMSE for the**  
 958 **comparison of the eight BB scenarios, (c)-1 to (c)-8 are the R for the comparison of the eight BB scenarios.**



959



960

961

962

963

964

965

**Figure 7. Time series of daily average AOD (550 nm) simulated by WRF-Chem including 8 BB emissions in March 2021 compared to 16 AERONET sites (a-p). These stations are divided into three categories, where the first category of stations is located within the HAOD range of satellite inversion (97-110°E, 15-22.5°N, a-g); The second type consists of observational sites located in adjacent high AOD regions (namely AHAOD, h-l); The third type encompasses observational sites situated within the downwind areas (namely DA, m-p). The legend line characterizes different BB simulation scenarios.**

966

967

968

969

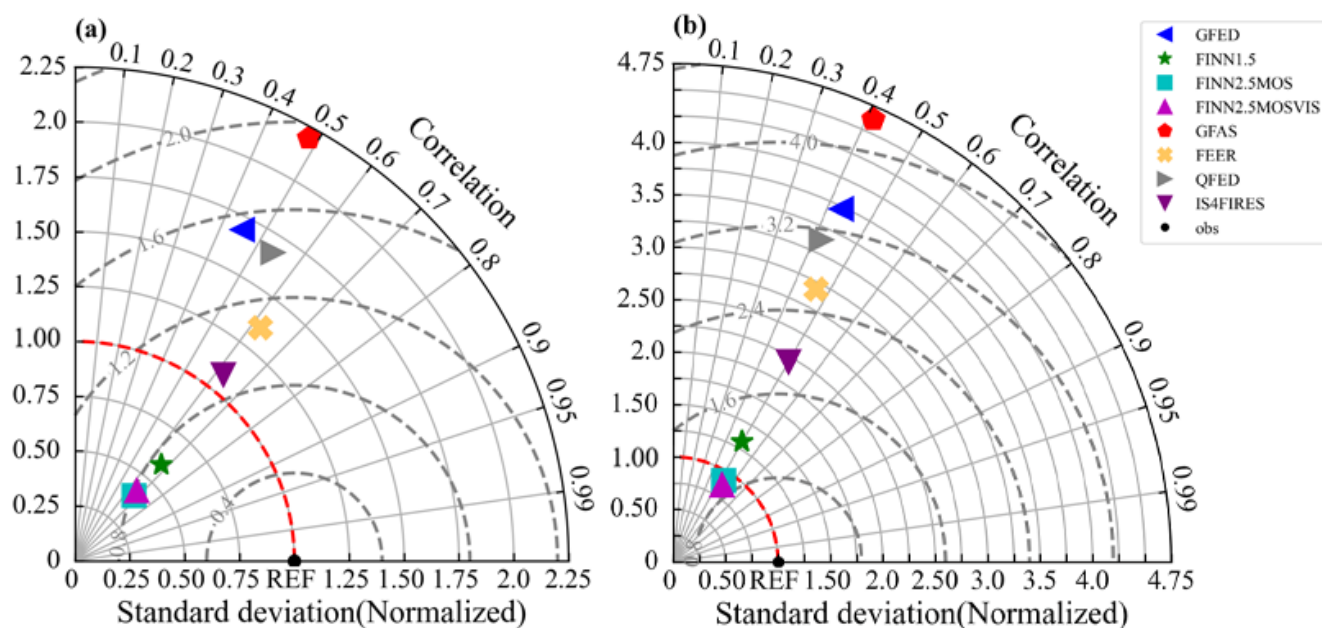
970

971

972



973



974

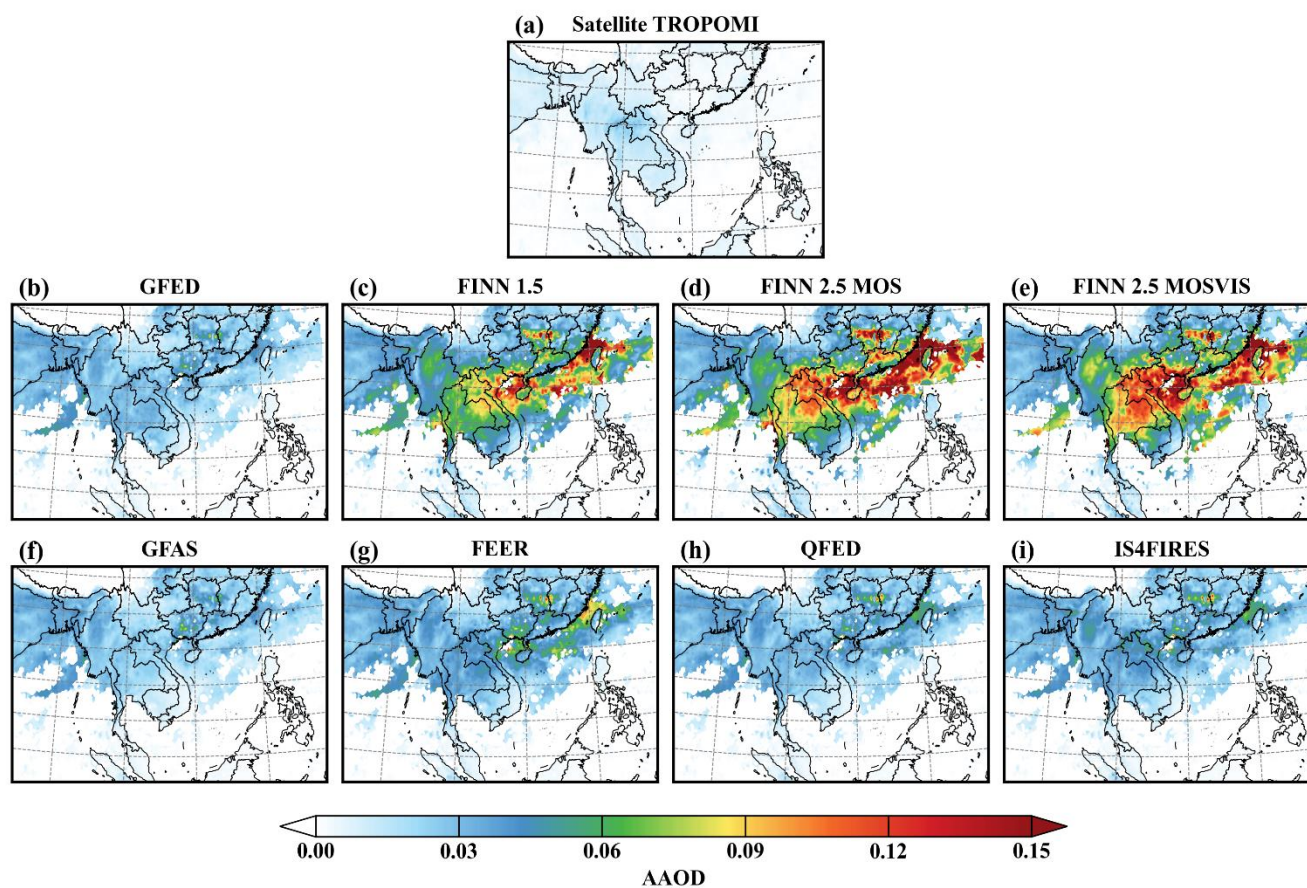
975

976

Figure 8. Taylor diagrams of (a) AERONET vs. WRF-Chem AOD at 550 nm and (b) AERONET vs. WRF-Chem AAOD at 500 nm in the HAOD region (97-110°E, 15-22.5°N) during the wildfire period.

977





978

979 **Figure 9. Spatial distribution of AAOD between Sentinel-5 TROPOMI satellite (a) vs. AAOD simulated by WRF-Chem with 8 BB**  
980 **emission inventories (b-i) during wildfire period in PSEA.**

981

982

983

984

985

986

987

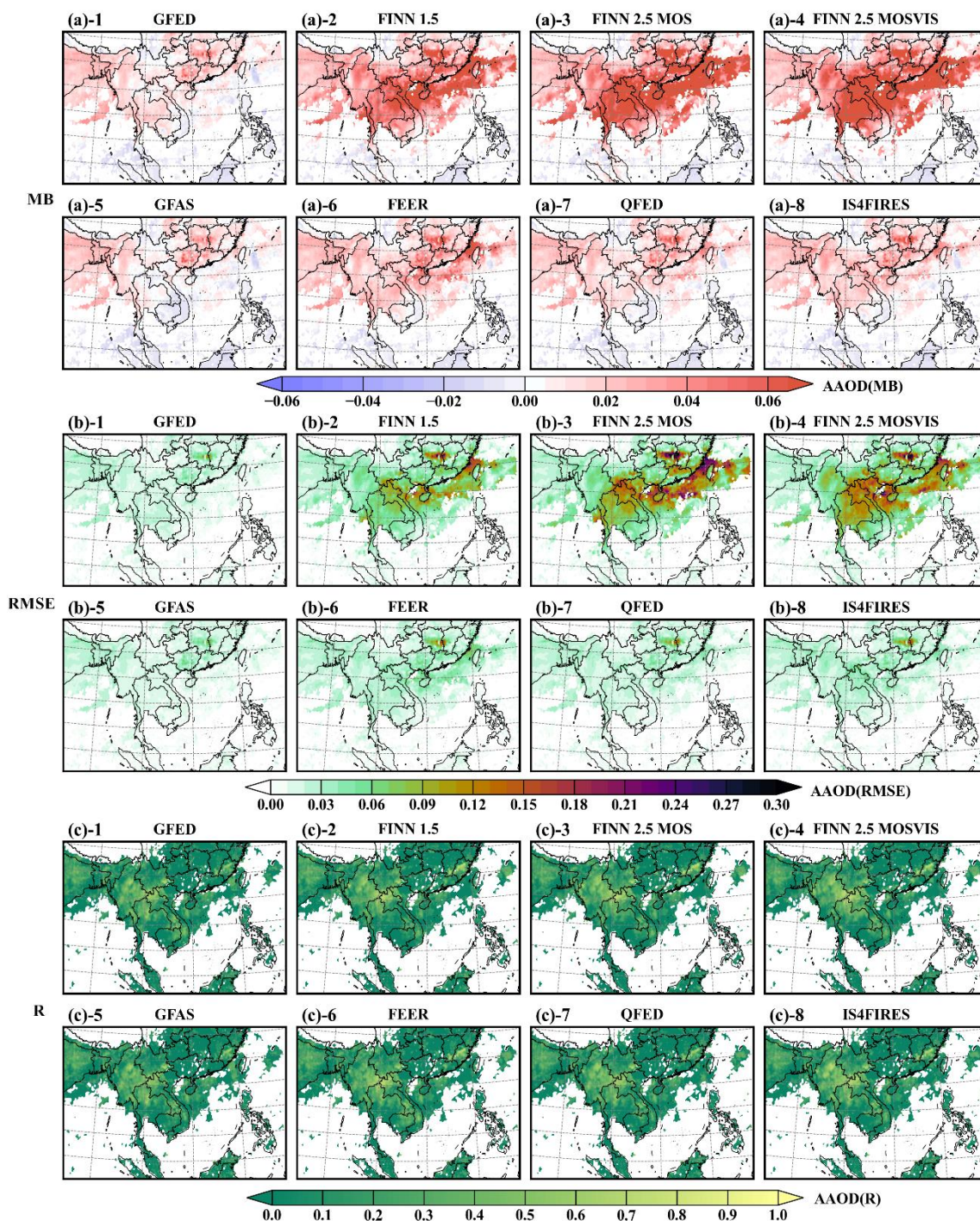
988

989

990

991

992



993

994

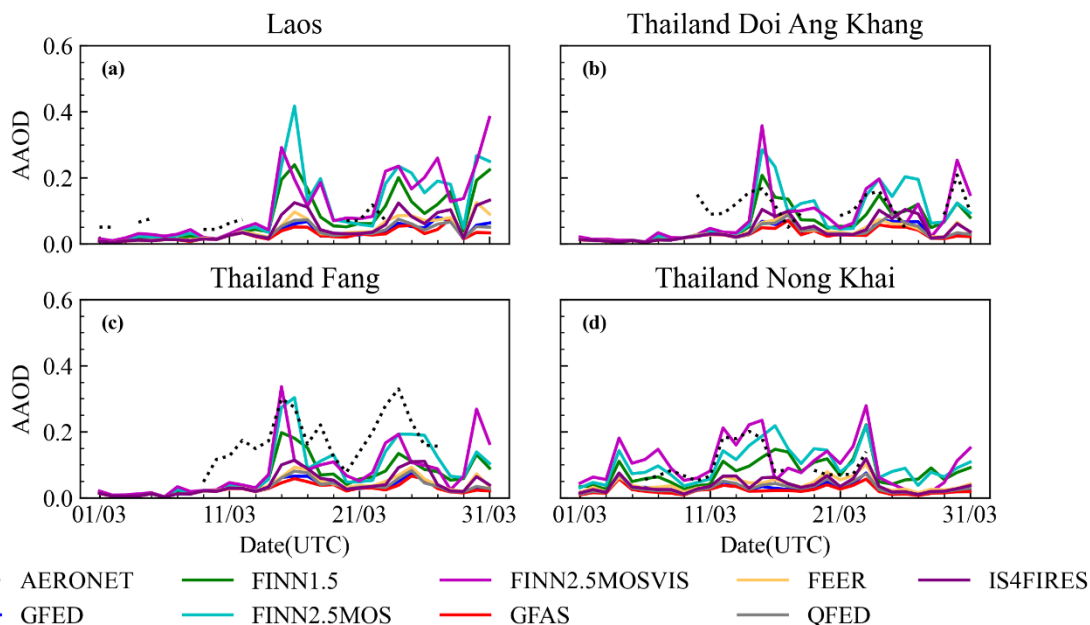
995

996

997

Figure 10. Spatial distribution of MB, RMSE, and R between AOD from VIIRS satellite vs. AOD simulated by WRF-Chem with 8 BB emission inventories (GFED, FINN1.5, FINN2.5 MOS, FINN2.5 MOSVIS, GFAS, FEER, QFED, IS4FIRES) in PSEA during March 2019, where (a)-1 to (a)-8 are the MB for the comparison of the eight BB scenarios, (b)-1 to (b)-8 are the RMSE for the comparison of the eight BB scenarios, (c)-1 to (c)-8 are the R for the comparison of the eight BB scenarios.





998

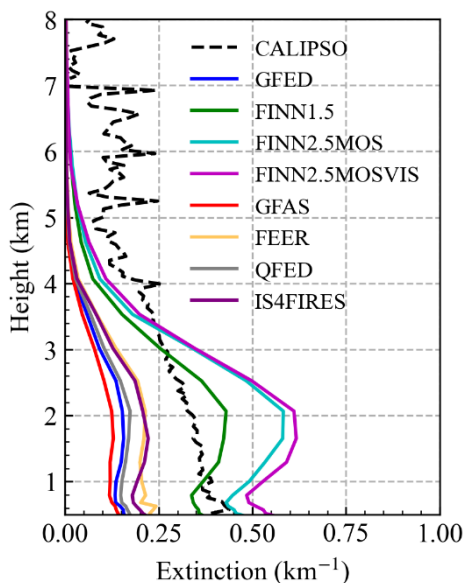
999

1000

1001

1002

**Figure 11.** Comparisons of time series between daily mean AAOD at 500 nm measurements provided by four AERONET sites within the HAOD range and AAOD simulated by the nearest corresponding AERONET site using WRF-Chem adding different BB inventories, where the satellite inversions of both AOD > 1 and AAOD > 0.03 range 97-110°E, 15-22.5°N are called HAOD. The legend line is the same as in Figure 7.



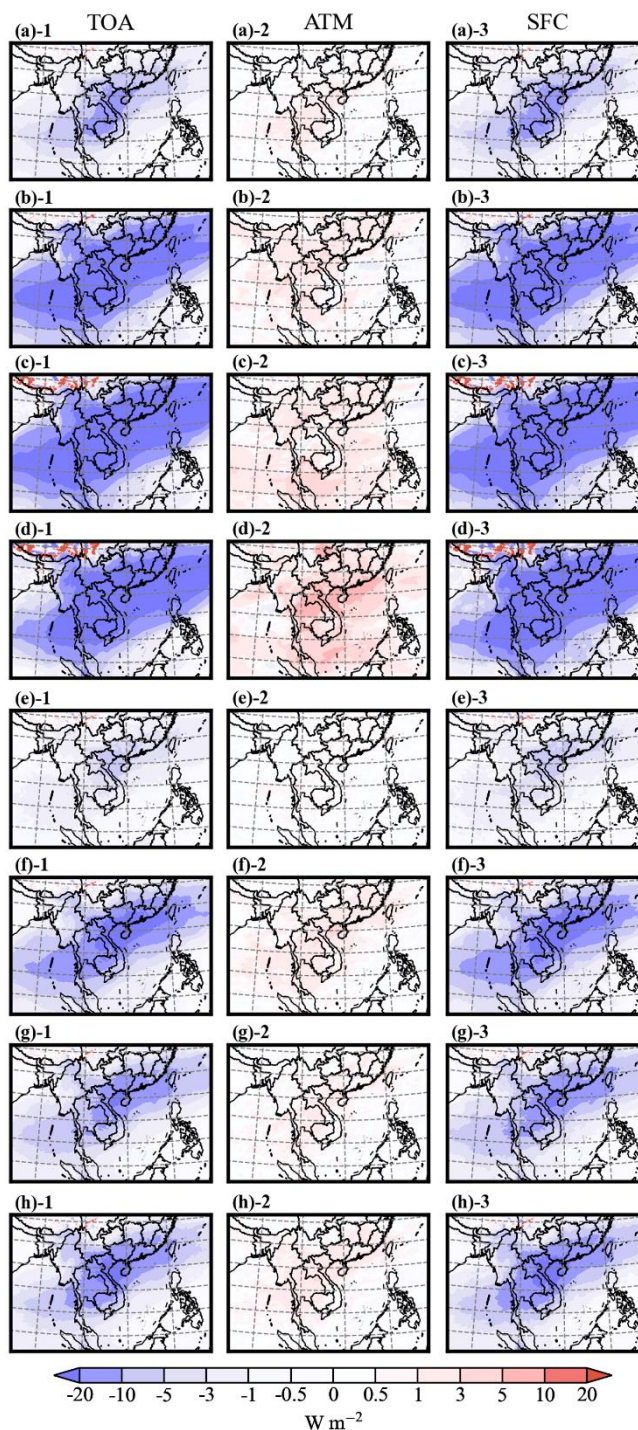
1003

1004

1005

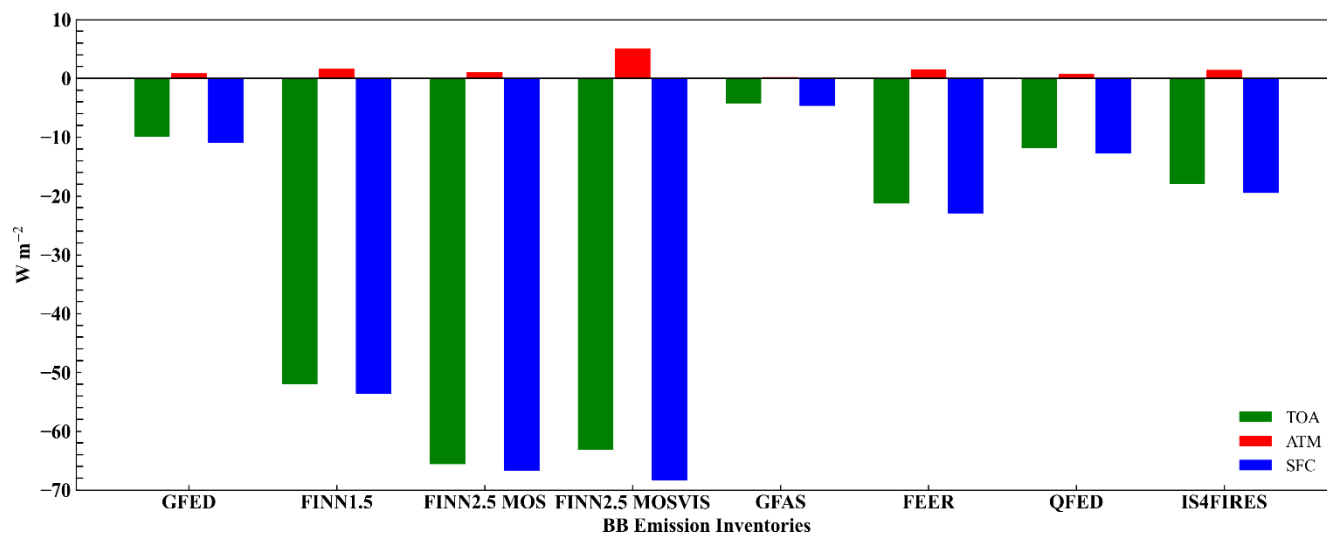
1006

**Figure 12.** Vertical distributions of monthly mean aerosol extinction (550 nm) from WRF-Chem with different BB inventories and the corresponding CALIPSO retrieval (532nm) in HAOD (97-110°E, 15-22.5°N). The black dotted line indicates CALIPSO and the remaining lines are the same as in Figure 7.



1007  
 1008  
 1009  
 1010

**Figure 13.** The average difference in clear-sky SW radiation fluxes (daytime) simulated with and without BB emission (GFED, FINN1.5, FINN2.5 MOS, FINN2.5 MOSVIS, GFAS, FEER, QFED, IS4FIRES) over the PSEA in March 2019 at the top of the atmosphere (TOA), ground surface (SFC), and in the atmosphere (ATM), Where (a)-(h) represent 8 emission inventories.



1011

1012

1013

**Figure 14.** The average difference in clear-sky SW radiation fluxes (daytime) simulated with and without BB emission in the HAOD (97-110°E,15-22.5°N) region during March 2019.

1014